The Astronomical Journal, 156:298 (25pp), 2018 December https://doi.org/10.3847/1538-3881/aaee89

The *HST* PanCET Program: Hints of Na I and Evidence of a Cloudy Atmosphere for the Inflated Hot Jupiter WASP-52b

Munazza K. Alam[1,14], Nikolay Nikolov[2], Mercedes López-Morales[1], David K. Sing[2,3], Jayesh M. Goyal[2], Gregory W. Henry[4], Jorge Sanz-Forcada[5], Michael H. Williamson[4], Thomas M. Evans[2], Hannah R. Wakeford[6], Giovanni Bruno[6,7], Gilda E. Ballester[8], Kevin B. Stevenson[6], Nikole K. Lewis[6,9], Joanna K. Barstow[10], Vincent Bourrier[11], Lars A. Buchhave[12], David Ehrenreich[11], and Antonio García Muñoz[13]
[1] Department of Astronomy, Harvard-Smithsonian Center for Astrophysics, Cambridge, MA 02138, USA; munazza.alam@cfa.harvard.edu
[2] Astrophysics Group, School of Physics and Astronomy, University of Exeter, Exeter EX4 4QL, UK
[3] Department of Earth and Planetary Sciences, Johns Hopkins University, Baltimore, MD 21218, USA
[4] Center of Excellence in Information Systems, Tennessee State University, Nashville, TN 37209, USA
[5] Centro de Astrobiología (CSIC-INTA), ESAC Campus, Villanueva de la Cañada, Madrid, Spain
[6] Space Telescope Science Institute, Baltimore, MD 21218, USA
[7] INAF-Osservatorio Astrofisico di Catania, via S. Sofia, 78, I-95123 Catania, Italy
[8] Lunar and Planetary Laboratory, University of Arizona, Tucson, AZ 85721, USA
[9] Department of Astronomy and Carl Sagan Institute, Cornell University, Ithaca, NY 14853, USA
[10] Department of Physics and Astronomy, University College London, London WC1E 6BT, UK
[11] Observatoire de l'Université de Genève, Sauverny, Switzerland
[12] DTU Space, National Space Institute, Technical University of Denmark, Lyngby, Denmark
[13] Zentrum für Astronomie und Astrophysik, Technische Universität Berlin, Berlin, Germany
Received 2018 June 8; revised 2018 October 10; accepted 2018 November 1; published 2018 December 6

Abstract

We present an optical to near-infrared transmission spectrum of the inflated hot Jupiter WASP-52b using three transit observations from the Space Telescope Imaging Spectrograph mounted on the *Hubble Space Telescope*, combined with *Spitzer*/Infrared Array Camera photometry at 3.6 and 4.5 μm. Since WASP-52 is a moderately active ($\log(L_x/L_{bol}) = -4.7$) star, we correct the transit light curves for the effect of stellar activity using ground-based photometric monitoring data from the All-sky Automated Survey for Supernovae (ASAS-SN) and Tennessee State University's Automatic Imaging Telescope. We bin the data in 38 spectrophotometric light curves from 0.29 to 4.5 μm and measure the transit depths to a median precision of 90 ppm. We compare the transmission spectrum to a grid of forward atmospheric models and find that our results are consistent with a cloudy spectrum and evidence of sodium at 2.3σ confidence, but we find no observable evidence of potassium absorption even in the narrowest spectroscopic channel. We find that the optical transmission spectrum of WASP-52b is similar to that of the well-studied inflated hot Jupiter HAT-P-1b, which has comparable surface gravity, equilibrium temperature, mass, radius, and stellar irradiation levels. At longer wavelengths, however, the best-fitting models for WASP-52b and HAT-P-1b predict quite dissimilar properties, which could be confirmed with observations at wavelengths longer than $\sim$1 μm. The identification of planets with common atmospheric properties and similar system parameters will be insightful for comparative atmospheric studies with the *James Webb Space Telescope*.

Key words: planets and satellites: atmospheres – planets and satellites: composition – planets and satellites: individual (WASP-52b)

1. Introduction

Transiting exoplanets offer unprecedented opportunities for the detection and detailed characterization of planets beyond the solar system (Struve 1952). From transit observations, we can make inferences about the formation and evolutionary histories of these planets, their bulk compositions, and their atmospheres (Winn 2010). Atmospheric studies can be performed using transmission spectroscopy to constrain atmospheric structure and chemical composition (e.g., Charbonneau et al. 2002; Vidal-Madjar et al. 2003; Wakeford et al. 2017), secondary eclipses to measure temperature and thermal structure (e.g., Deming et al. 2005; Charbonneau et al. 2008; Sing & López-Morales 2009; Evans et al. 2017), and orbital phase curves to probe atmospheric circulation (e.g., Knutson et al. 2007; Stevenson et al. 2017). The subject of this paper is transmission spectroscopy (Seager & Sasselov 2000; Brown 2001). During transit, light from the host star passes through the atmosphere of the planet. At wavelengths where absorption by atoms, molecules, and aerosols takes place, the planet blocks slightly more stellar flux, resulting in variations in the apparent radius of the planet as a function of wavelength. These variations in planetary radius reveal the composition of the planetary atmosphere.

The gaseous atmospheres of short-period hot Jupiters are most accessible to such observations because of their large scale heights and short orbital periods. Narrow peaks of H I (1215 Å) in the ultraviolet (UV), Na I (5893 Å) and K I (7665 Å) in the optical, H_2O (1.4 μm; 1.9 μm), CO (2.3 μm; 4.7 μm), CO_2 (2 μm; 15 μm), and CH_4 (2.2 μm; 7.5 μm) in the near-infrared (NIR), and scattering by molecular hydrogen (H_2) are expected to be prominent features in clear hot Jupiter

[14] National Science Foundation Graduate Research Fellow.

Table 1
Transit Observations of WASP-52b

Obs. date	Visit number	Telescope/Instrument	Grating/Grism	Number of images	Exposure time (s)
UT 2016 Nov 1	52	*HST*/STIS	G430L[a]	37	253
UT 2016 Nov 29	53	*HST*/STIS	G430L[a]	37	253
UT 2017 May 11	54	*HST*/STIS	G750L[b]	37	253
UT 2016 Oct 18	···	*Spitzer*/IRAC	[3.6 μm]	28800	1.92
UT 2018 Mar 22	···	*Spitzer*/IRAC	[4.5 μm]	29300	1.98

Notes.
[a] Central wavelength: 4300 Å.
[b] Central wavelength: 7751 Å.

atmospheres (Seager & Sasselov 2000; Sudarsky et al. 2003; Vidal-Madjar et al. 2003; Burrows et al. 2010; Fortney et al. 2010). Charbonneau et al. (2002) detected the first exoplanet atmosphere for the hot Jupiter HD 209458b, which was later confirmed to have absorption from Na I, H_2 Rayleigh scattering, and possible TiO/VO absorption (Désert et al. 2008; Lecavelier Des Etangs et al. 2008; Sing et al. 2008a, 2008b; Snellen et al. 2008). The first near-UV to IR (0.3–8.0 μm) transmission spectrum of the hot Jupiter HD 189733b (Pont et al. 2013) revealed clouds or hazes consistent with Rayleigh scattering by small condensate particles in addition to narrow peaks of Na I and K I, H_2O absorption, and an escaping H atmosphere (Grillmair et al. 2008; Sing et al. 2009; Lecavelier Des Etangs et al. 2010; Bourrier et al. 2013).

To date, a diversity of hot Jupiters with a continuum of clear to cloudy atmospheres (Sing et al. 2016) has been detected, with no apparent correlation between the observed spectra and other system parameters. Space-based atmospheric studies have yielded detections of Na I and K I (e.g., Charbonneau et al. 2002; Nikolov et al. 2014), elucidated the presence of thick atmospheric cloud decks (e.g., Sing et al. 2015), and provided water abundance constraints (e.g., Kreidberg et al. 2014; Wakeford et al. 2018). From ground-based transmission spectral surveys of hot Jupiters, we have detected Na I (e.g., Wyttenbach et al. 2015, 2017; Nikolov et al. 2016, 2018), K I (e.g., Sing et al. 2011a; Nikolov et al. 2016), cloudy/hazy atmospheres (e.g., Jordán et al. 2013; Mallonn et al. 2016; Huitson et al. 2017), and Rayleigh scattering slopes (e.g., Gibson et al. 2017).

Here we present results for WASP-52b (Hébrard et al. 2013) from the *Hubble Space Telescope* (*HST*) Panchromatic Comparative Exoplanetology Treasury (PanCET) program (GO 14767; PIs Sing & López-Morales). The scientific goals of PanCET are to provide a uniform, statistically compelling UV through IR study of clouds/hazes and chemical composition in exoplanet atmospheres, and assemble a UVOIR legacy sample of exoplanet transmission spectra that will be well suited for follow-up with the *James Webb Space Telescope (JWST)*.

WASP-52b is a 0.46 $M_{\rm Jup}$ and 1.27 $R_{\rm Jup}$ inflated hot Jupiter ($T_{\rm eq} = 1300$ K) orbiting a moderately active ($\log(R'_{HK}) = -4.4 \pm 0.2$, Hébrard et al. 2013; $\log(L_{\rm x}/L_{\rm bol}) = -4.7$, Section 3.2) K2V star with a period of 1.75 days (Hébrard et al. 2013). This planet, at a spectroscopic parallax distance of 175.7 ± 1.3 pc (Gaia Collaboration et al. 2018), is a favorable target for atmospheric studies via transmission spectroscopy because of its large scale height ($H = 700$ km) and deep transit ($\delta = 0.028$). Based on its surface gravity ($\log(g) = 2.87$ dex) and equilibrium temperature ($T_{\rm eq} = 1315$ K), WASP-52b is predicted to have a predominantly cloudy atmosphere with muted spectral features (Stevenson 2016). However, two recent ground-based atmospheric analyses of this target claim discrepant conclusions. Louden et al. (2017) cite an optically thick cloud deck to explain an observed flat transmission spectrum, but note that their results are inconsistent with deeper transit depths at longer wavelengths (Kirk et al. 2016). Conversely, Chen et al. (2017) report a cloudy atmosphere with a noticeable Na I detection and a weaker detection of K I absorption.

In this work, we measure WASP-52b's transmission spectrum over the ∼0.29–4.5 μm wavelength range by combining *HST*/Space Telescope Imaging Spectrograph (STIS) and *Spitzer*/Infrared Array Camera (IRAC) observations. An outline of the paper is as follows. In Section 2, we describe the observations and data reduction techniques. In Section 3, we detail the stellar activity correction. The light curve fits and measurement of the transmission spectrum are described in Section 4. We compare our results to previously published measurements and to a grid of forward atmospheric models in Section 5, and we present an interpretation of the transmission spectrum in Section 6. We summarize the paper in Section 7.

2. Observations and Data Reduction

2.1. Observations

We obtained time series spectroscopy during three transits of WASP-52b with *HST*/STIS on UT 2016 November 1 and UT 2016 November 29 using the G430L grating (2892–5700 Å) and UT 2017 May 11 using the G750L grating (5240–10270 Å). Two additional transits were observed with *Spitzer*/IRAC as part of GO program 13038 (PI Stevenson) in the 3.6 μm channel on UT 2016 October 18 and in the 4.5 μm channel on UT 2018 March 22. Table 1 summarizes the transit observations and instrument settings for each visit.

2.1.1. HST/*STIS*

The G430L and G750L STIS data have resolving power $R \sim 500$, and each set consists of 37 stellar spectra taken over four consecutive 96-minute orbits. The visits were scheduled to include the transit event in the third orbit, providing an out-of-transit baseline time series before and after the transit, as well as good coverage between the second and third contact. We used a 128-pixel-wide subarray and exposure times of 253 s to reduce the readout times between exposures. To minimize slit losses, the data were taken with the 52 × 2 arcsec^2 slit.

2.1.2. Spitzer/*IRAC*

Two transits of WASP-52b were observed on UT 2016 October 18 and UT 2018 March 22 with the *Spitzer* space

telescope (Werner et al. 2004) using the 3.6 and 4.5 μm IRAC channels (Fazio et al. 2004). Although these observations cover the complete phase curve of the planet, for this work we only use a 6 hr portion of the phase curve centered on the transit event with enough out-of-transit baseline flux to allow for accurate analysis. Each IRAC exposure had an effective integration time of ~2 s, resulting in ~30,000 images for the portion of the phase curve corresponding to the transit.

2.2. Data Reduction

2.2.1. HST/*STIS*

We reduced (bias-, dark-, and flat-corrected) the raw 2D G430L and G750L spectra using the `CALSTIS`[15] pipeline (version 3.4) and the relevant calibration frames. Following the procedure detailed in Nikolov et al. (2014), we used median-combined difference images to identify and correct for cosmic-ray events and bad pixels flagged by `CALSTIS`. We extracted 1D spectra from the calibrated `.flt` science files using IRAF's `APALL` task. To identify the most appropriate aperture, we extracted light curves of aperture widths ranging from 6 to 18 pixels with a step size of 1. We defined the best aperture for each grating according to the lowest photometric dispersion in the out-of-transit baseline flux. Based on this criterion, we used an aperture size of 13 pixels in our analysis. For each exposure, we computed the midexposure time in MJD.

Aperture extractions with no background subtraction minimize the out-of-transit standard deviation of the white light curves (Sing et al. 2015). Although the STIS 2D spectra are known to show negligible background sky contribution (Sing et al. 2011b, 2013; Huitson et al. 2012, 2013; Nikolov et al. 2015; Gibson et al. 2017), we assessed the potential bias of the sky background on the light curves by obtaining time series spectroscopy both with and without background subtraction. Comparing the light curves, we find that both data sets are fully consistent. To obtain a wavelength solution, we used the `x1d` files from `CALSTIS` to resample all of the extracted spectra and cross-correlate them to a common rest frame. The cross-correlation measures the shift, and the spectra are resampled to align them and remove subpixel drifts in the dispersion direction. These drifts can be associated with the different locations of the spacecraft on its orbit around the Earth (e.g., Huitson et al. 2013).

2.2.2. Spitzer/*IRAC*

We analyzed the IRAC photometry following the methodology of Nikolov et al. (2015) and Sing et al. (2015, 2016). We started our analysis using the Basic Calibrated Data (`.bcd`) files and converted the images from flux in mega-Jansky per steradian (MJy sr^{-1}) to photon counts (i.e., electrons) by multiplying each image by the gain and exposure time and then dividing by the flux conversion factor. Following the reduction procedure outlined in Knutson et al. (2012) and Todorov et al. (2013), we filtered for outliers (hot or lower pixels in the data) by following each pixel in time. We scanned the images in two passes: first by removing outliers $\geqslant 8\sigma$ away from the median value of each frame compared to the 10 surrounding images and then by removing outliers above the 4σ level following the same procedure. The total fraction of corrected pixels was 0.05%.

We estimated and subtracted the sky background for each image using an iterative 3σ clipping procedure in which we excluded all pixels associated with the stellar point-spread function (PSF), background stars, or hot pixels. In the last iteration, we created a histogram from the remaining pixels and determined the sky background based on a Gaussian fit to the distribution of remaining pixels. To locate the center of the PSF for each image, we used the flux-weighted centroiding method with a 5-pixel-radius circular region centered on the approximate position of the star. The variation of the x and y positions of the PSF on the detectors was measured to be 0.19 and 0.24 pixels, respectively.

We extracted photometric points following fixed and time-variable photometry. In the fixed approach, we used circular apertures ranging in radius from 4 to 8 pixels in increments of 0.5. For the time-variable photometry, the aperture size was scaled by the value of the noise pixel parameter (the normalized effective background area of the IRAC point response function), which depends on the FWHM of the stellar PSF squared (Mighell 2005; Knutson et al. 2012; Lewis et al. 2013; Nikolov et al. 2015). We identified the best results from both photometric methods by comparing the light curve residual dispersion, as well as the white and red noise components measured with the wavelet technique detailed in Carter & Winn (2009). The time-variable method resulted in the lowest white and random red noise correlated with data points coadded in time.

Table 2
Summary of Photometric Observations for WASP-52b

Observing season	N_{obs}	Date range (HJD-2,450,000)	Sigma (mag)	Seasonal mean (mag)
		AIT		
2014–2015	61	56943–57066	0.14288	0.01270
2015–2016	48	57293–57418	0.15069	0.00892
2016–2017	27	57705–57785	0.16062	0.01335
		ASAS-SN		
2013–2014	154	56638–57031	0.16692	0.01162
2014–2015	175	57145–57385	0.15601	0.01558
2015–2016	209	57507–57749	0.11866	0.01195
2016–2017	202	57878–58115	0.11769	0.01167

3. Stellar Activity Correction

Since WASP-52 is a moderately active star ($\log(R'_{HK}) = -4.4 \pm 0.2$, Hébrard et al. 2013), we used ground-based activity monitoring data to track stellar activity levels during the epochs of our transits. Before fitting the transit light curves, we corrected the baseline flux levels for the effect of stellar variability using a quasi-periodic Gaussian process (GP) regression model and corrected for the effect of unocculted stellar spots following the prescription of Huitson et al. (2013). Table 2 summarizes the photometric monitoring campaigns (from the All-sky Automated Survey for Supernovae (ASAS-SN) and Tennessee State University's Automatic Imaging Telescope (AIT)), and Table 3 includes the average flux correction for our transit observations.

[15] http://www.stsci.edu/hst/stis/software/analyzing/calibration/pipe_soft_hist/intro.html

Table 3
Stellar Flux Values (Normalized by the Nonspotted Stellar Flux) for Each Transit Observation and Average Flux Correction for Each Bandpass

Instrument	$f_{\rm norm}$	Error	Δf
STIS (visit 52)	0.978	0.009	0.039
STIS (visit 53)	0.955	0.016	0.039
STIS (visit 54)	0.972	0.016	0.022
IRAC	0.959	0.009	0.006

3.1. Stellar Variability Monitoring

We acquired 135 out-of-transit *R*-band images over the 2014–2015, 2015–2016, and 2016–2017 observing seasons with Tennessee State University's 14 inch Celestron Automatic Imaging Telescope. These observations, however, do not include the epochs of the *Spitzer* and ground-based (Chen et al. 2017; Louden et al. 2017) transit observations. We therefore used 740 out-of-transit *V*-band images from Ohio State University's All-sky Automated Survey for Supernovae[16] program (Shappee et al. 2014; Kochanek et al. 2017) for more detailed activity monitoring coverage. The ASAS-SN observations were taken over the 2013–2014, 2014–2015, 2015–2016, and 2016–2017 observing seasons. The number of observations, date range, mean magnitude, and standard deviation of the data taken in each observing season are included in Table 2.

3.2. Estimating Activity Levels

To quantify the level of activity in WASP-52, we used observations from the Advanced CCD Imaging Spectrometer (ACIS) on the *Chandra* X-ray telescope. These data were taken from the *Chandra* public archive (GO 15728; PI Wolk). Standard CIAO[17] tasks were applied to reduce the data. The software ISIS (Houck & Denicola 2000) was used to fit the spectrum with a metallicity fixed to photospheric values ([Fe/H] = 0.03), and the interstellar matter (ISM) absorption was assumed to be $N_{\rm H} = 4 \times 20\,{\rm cm}^{-3}$ (based on target location and distance), consistent with the fit. The resulting $1-T$ fit has $\log T({\rm K}) = 6.54^{+1.06}_{-0.29}$ and $\log {\rm EM}\ ({\rm cm}^{-3}) = 51.14^{+0.33}_{-0.63}$. We measured an X-ray luminosity of $L_{\rm x} = (3.5 \pm 1.0) \times 10^{28}$ erg s^{-1} in the 0.12–2.48 keV band (J. Sanz-Forcada et al. 2018, in preparation). The light curve shows variability, but poor statistics hamper a detailed analysis. The corresponding $\log(L_{\rm x}/L_{\rm bol}) = -4.7$ indicates that WASP-52 is a moderately active star. Further details will be included in J. Sanz-Forcada et al. (2018, in preparation).

3.3. Modeling the Variability Monitoring Data

We initially adopted a simple sinusoidal model of period $P = 11.8 \pm 3.3$ days based on the Hébrard et al. (2013) rotational period, but we found that this approach did not accurately model the variations in amplitude and period of the AIT and ASAS-SN variability monitoring data over all observing seasons. Discrepancies between the sinusoidal model and the photometric monitoring data are likely due to different spot configurations at different observed epochs (Dang et al. 2018), suggesting that a quasi-periodic model would more accurately fit the data.

We therefore jointly modeled the AIT and ASAS-SN ground-based stellar activity data using a GP regression, a framework that has been shown to accurately disentangle stellar activity signals from planetary signals in radial velocity data (e.g., Aigrain et al. 2012; Haywood et al. 2014) and photometry (e.g., Pont et al. 2013; Aigrain et al. 2016; Angus et al. 2018). We ran a GP optimization routine (Ambikasaran et al. 2015) using the `George` package for Python. We used a three-component kernel to model the quasi-periodicity of the ground-based activity monitoring data, irregularities in the amplitude of the ground-based photometry, and stellar noise. See Appendix A.1 for further details regarding the functional form of our chosen kernel. We use a gradient-based optimization routine to find the best-fit hyperparameters and set the 11.8 ± 3.3 day rotation period from Hébrard et al. (2013) as a uniform prior with an uncertainty three times larger than the literature value. Figure 1 shows the ground-based variability monitoring data overplotted with the GP model for all seasons modeled jointly and for each observing season separately.

The GP regression model with a quasi-periodic kernel reproduces the observed flux variations well for epochs during which we have stellar activity data, but has large uncertainties outside of a given season. The model accurately predicts the stellar activity behavior for each observing season when fit separately, but this model prediction has a significantly larger 1σ uncertainty when fitting the data from all seasons together. We therefore modeled the data for each observing season separately, and we used the amplitude of the photometric variation given by the GP model for each epoch to correct the transmission spectrum for the effects of stellar activity (see Section 3.4).

3.4. Correcting for Unocculted Spots

The temperature difference between the stellar photosphere and the spotted region introduces a slope in the planet spectrum (e.g., Kreidberg 2017), so it is necessary to correct for this effect. Using the results of the GP regression model described in Section 3.3, we followed the prescription of Huitson et al. (2013) to correct the spectrophotometric light curves for the effect of unocculted stellar spots of a fixed size. This method involves estimating the variability amplitude for a broadband wavelength value (determined by the photometric filter of the activity monitoring data), which can then be used as an anchor for the wavelength-dependent flux correction on the *HST* and *Spitzer* data.

We first converted the ASAS-SN and AIT photometric variability monitoring data to relative flux. Excluding in-transit measurements, we estimated the nonspotted stellar flux to be $F_\star = \max(F) + k\sigma$, where F is the variability monitoring data, σ is the dispersion of the photometric measurements, and k is a factor fixed to unity (Aigrain et al. 2012; see also Appendix A.2). The variability monitoring data were then normalized to the nonspotted stellar flux to estimate the amount of dimming. Table 3 gives the dimming values for each transit observation. We also computed the amplitude of the spot corrections at the variability monitoring wavelength $\Delta f_0 = 1 - f_{\rm norm}$, where $f_{\rm norm}$ is the mean of the normalized flux array.

To derive the wavelength-dependent flux correction, we used a stellar flux model ($T_{\rm eff} = 5000$ K, $\log(Z) = -1.5$, $\log(g) = 4.5$) and a spot model ($T_{\rm eff} = 4750$ K, $\log(Z) = -1.5$, $\log(g) = 4.5$)

[16] https://asas-sn.osu.edu/
[17] CIAO (*Chandra* Interactive Analysis of Observations) 4.9 and CALDB 4.7.4 versions were used in the analysis (Fruscione et al. 2006).

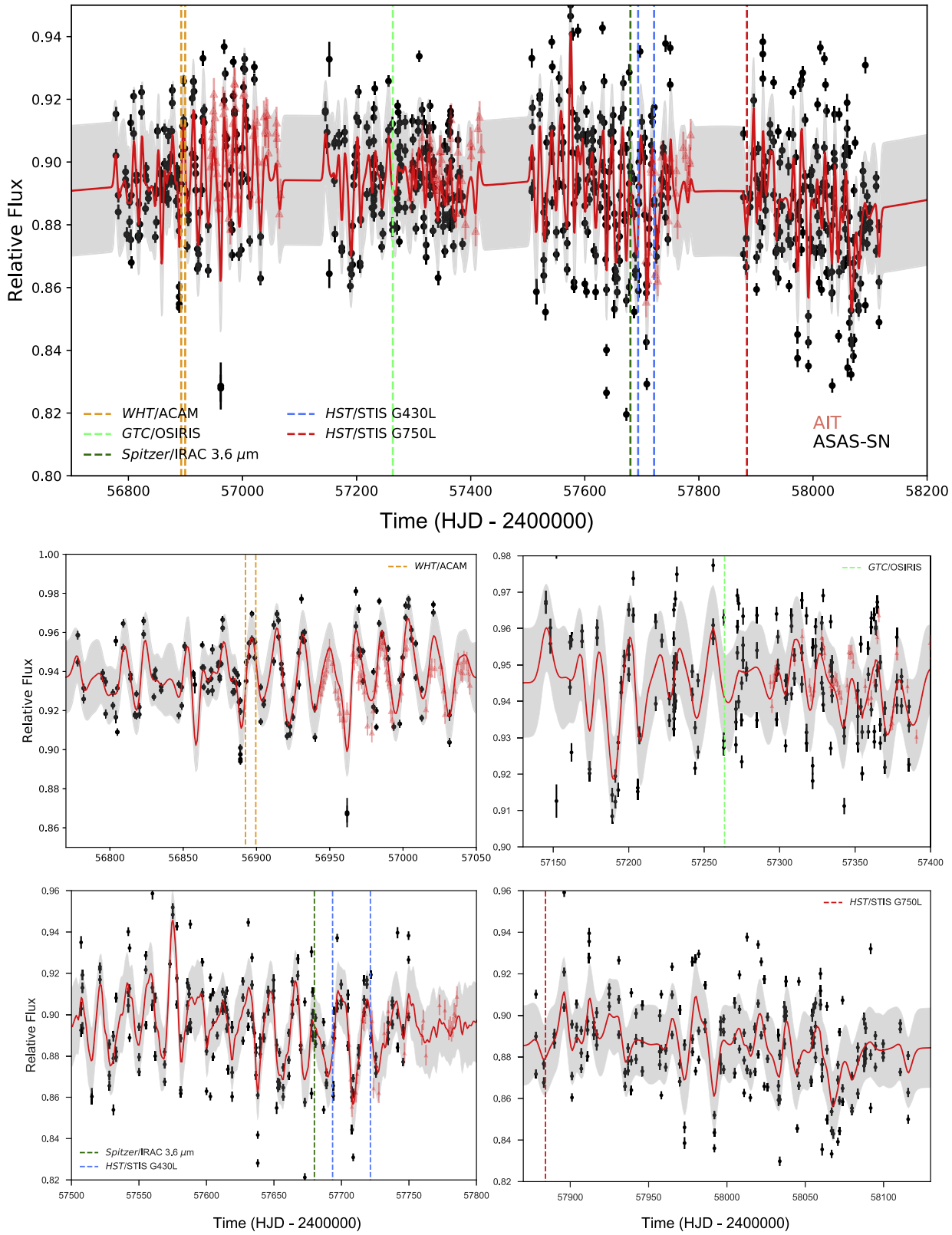

Figure 1. Ground-based photometric observations of WASP-52 from ASAS-SN (black points) and AIT (red triangles) during the 2013–2014 (middle left), 2014–2015 (middle right), 2015–2016 (bottom left), and 2016–2017 (bottom right) observing seasons. The data are flux relative to the average brightness of comparison stars. The Gaussian process regression model (red) and 1σ uncertainty (gray) fits to the combined ASAS-SN and AIT data are overplotted for the full data set (top panel) and for each observing season separately. The dashed vertical lines indicate the *WHT*/ACAM (orange), *GTC*/OSIRIS (light green), *HST*/STIS G430L (blue), *HST*/STIS G750L (red), and *Spitzer*/IRAC (dark green) transit epochs.

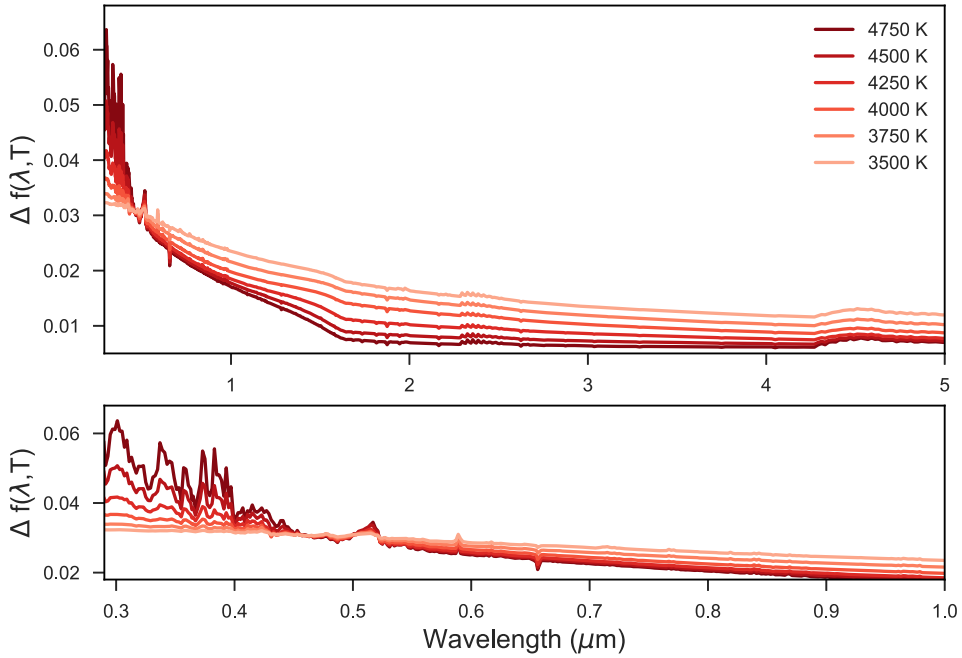

Figure 2. Theoretical dimming of unocculted spots in the wavelength range of the *HST*/STIS and *Spitzer*/IRAC observations for stellar flux models ranging in temperature from 3500 to 4750 K (corresponding to temperature differences between the spot and stellar photosphere from 1500 K to 250 K). The dimming $\Delta f(\lambda, T)$ is derived by multiplying the wavelength-dependent flux correction by the nonspotted stellar flux (Section 3.4). Top panel: spot dimming for the full STIS+*Spitzer* wavelength range (~0.29–4.5 μm). Bottom panel: zoom-in of the STIS wavelength range only (~0.29–1.0 μm).

from the Kurucz (1993) 1D ATLAS grid[18] of stellar atmospheric models. The stellar flux model was chosen based on the effective temperature, metallicity, and surface gravity of WASP-52 given in Hébrard et al. (2013). The spot model is the same as the stellar model but 250 K cooler (Berdyugina 2005). To select this spot model, we tested different cold spots ranging from 3500 to 4750 K (corresponding to temperature differences between the spot and stellar photosphere from 1500 to 250 K). Figure 2 shows that spots at colder temperatures exhibit less flux dimming at longer wavelengths and a weaker slope in the optical. To correct for the effect of unocculted spots, we therefore use a spot model at 4750 K for which cold spots give the strongest slope to account for the maximum possible contribution from starspots in the data.

We interpolated the stellar model to the spot model grid and computed the wavelength-dependent correction factor derived in Sing et al. (2011b):

$$f(\lambda, T) = \left(1 - \frac{F_{\lambda, T_{\rm spot}}}{F_{\lambda, T_{\rm star}}}\right) \Bigg/ \left(1 - \frac{F_{\lambda_o, T_{\rm spot}}}{F_{\lambda_o, T_{\rm star}}}\right), \quad (1)$$

where $F_{\lambda, T_{\rm spot}}$ is the stellar model flux at temperature $T_{\rm spot}$ and at the wavelength of the transit observations, $F_{\lambda, T_{\rm star}}$ is the stellar model flux at the wavelength of the transit observations and at temperature $T_{\rm star}$, $F_{\lambda_o, T_{\rm spot}}$ is the stellar model flux at temperature $T_{\rm spot}$ at the reference wavelength of the activity monitoring data, and $F_{\lambda_o, T_{\rm star}}$ is the stellar model flux at temperature $T_{\rm star}$ at the activity monitoring reference wavelength. The final flux dimming correction was then calculated as $\Delta f = \Delta f_0 \times f(\lambda, T)$.

We computed the average flux correction over each bandpass (see Table 3) and applied the correction to each spectrophotometric light curve using

$$y_{\rm corrected} = y + \frac{\Delta f}{(1 - \Delta f)} \overline{y_{\rm oot}}, \quad (2)$$

where $y_{\rm corrected}$ is the corrected light curve flux, y is the original (uncorrected) light curve, and $\overline{y_{\rm oot}}$ is the mean of the out-of-transit exposures. We then fit analytic transit light curve models (Mandel & Agol 2002) to the stellar activity-corrected light curves, as detailed in Section 4.

4. Light Curve Fits

We extracted the broadband transmission spectrum and fit the spectrophotometric light curves following the methods described in Sing et al. (2011b, 2013) and Nikolov et al. (2014), and they are briefly summarized here. To simultaneously fit for the transit and systematic effects, we modeled each of the STIS and *Spitzer* transit light curves with a two-component function consisting of a transit model multiplied by a systematics model. We adopted the complete analytic transit models of Mandel & Agol (2002), which are parameterized by the midtransit time T_0, orbital period P, inclination i, normalized planet semimajor axis $a/R_\star$, and planet-to-star radius ratio $R_{\rm p}/R_\star$.

4.1. STIS White Light Curves

We produced the STIS broadband (wavelength-integrated) light curves by summing the time series over the complete wavelength range of the bandpass (2892–5700 Å for the G430L grating; 5240–10270 Å for the G750L grating). The white light curves for each of the STIS visits are shown in Figure 3. Photometric uncertainties were derived based on pure photon statistics. The raw white light curves exhibited instrumental systematics related to the orbital motion of the spacecraft

[18] http://kurucz.harvard.edu/

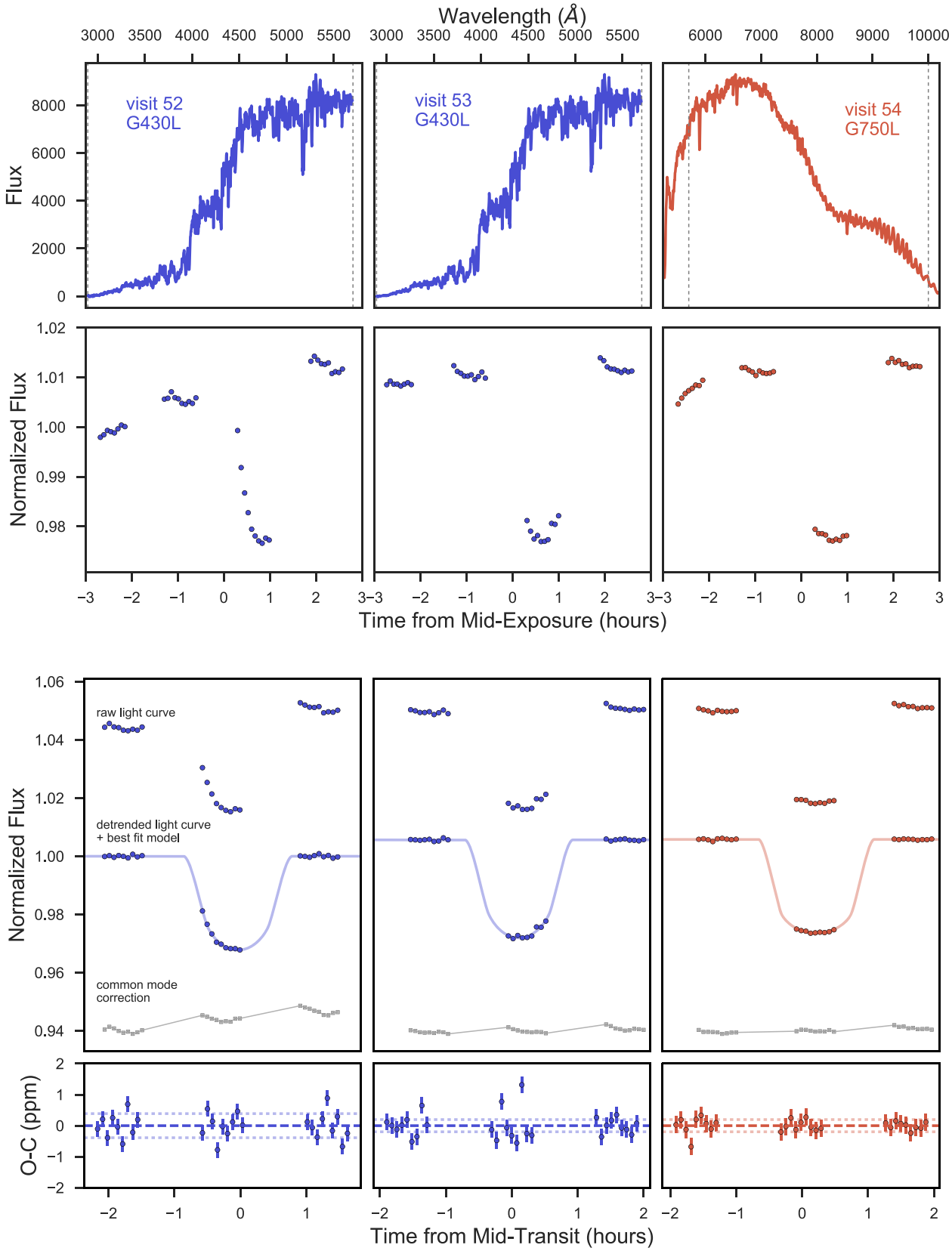

Figure 3. *HST*/STIS stellar spectra of WASP-52b and the corresponding white light curves for visits 52 (left column), 53 (middle column), and 54 (right column). Top panel: example stellar spectra taken with the G430L (blue) and G750L (red) grating. The vertical gray dashed lines indicate the wavelength range used to produce the white light curves. Second panel: the raw white light curves for each visit. Third panel: the raw and detrended light curves (excluding the first orbit and the first exposure of each subsequent orbit) with the best-fit model overplotted. The common mode correction (gray squares) is the transit+systematics model divided by the best-fit transit model. Bottom panel: transit fit residuals with error bars.

Table 4
Derived System Parameters for WASP-52b

	Hébrard et al. (2013)	Chen et al. (2017)	Louden et al. (2017)	This work[a]
Period P [days]	1.7497798 ± 0.0000012	1.7497798 (fixed)	1.74978089 ± 0.00000013	1.749779800 (fixed)
Orbital inclination i [°]	85.35 ± 0.20	85.06 ± 0.27	85.33 ± 0.22	85.17 ± 0.13
Orbital eccentricity e	0.0 (fixed)	0.0 (fixed)	0.0 (fixed)	0.0 (fixed)
Scaled semimajor axis $a/R_\star$	7.38 ± 0.10	7.14 ± 0.12	7.23 ± 0.12	7.22 ± 0.07
Radius ratio $R_p/R_\star$	0.1646 ± 0.0020	0.1608 ± 0.0018	0.1741 ± 0.0063	0.1639 ± 0.0005

Note.
[a] The values reported here are the weighted mean of fitted system parameters from the *Spitzer* observations.

(Gilliland et al. 1999; Brown 2001). In particular, the *HST* focus is known to experience significant variations on the spacecraft orbital timescale resulting from thermal expansion/contraction during the spacecraft's day/night orbital cycle.

As in past studies (e.g., Huitson et al. 2013; Sing et al. 2013; Nikolov et al. 2014), we accounted for and detrended these instrumental systematic effects by fitting a fourth-order polynomial to the flux dependence on *HST* orbital phase. We excluded the first orbit and the first exposure of each subsequent orbit in accordance with common practice, because these data have unique, complex systematics (see Figure 3) and were taken while the telescope was thermally relaxing into its new pointing position. We applied orbit-to-orbit flux corrections to the STIS data by fitting a polynomial of the spacecraft orbital phase (ϕ_t), drift of the spectra on the detector (x and y), the shift of each stellar spectrum cross-correlated with the first spectrum of the time series (ω), and time (t).

We then generated systematics models spanning all possible combinations of detrending variables (see Appendix B.1 and Table 7 for details) and performed separate fits using each systematics model included in the two-component function. For each model, we fixed P, i, and $a/R_\star$ to the values given in Hébrard et al. (2013), assumed zero eccentricity, and fit for T_0, $R_p/R_\star$, stellar baseline flux, and instrument systematic trends. We determined the best-fit parameters of the two-component model using a Levenberg–Marquardt least-squares fitting routine (Markwardt 2009) to derive the system parameters and calculated the Akaike Information Criterion (AIC; Akaike 1974) for each function. The results of these fits are shown in Table 4. The STIS stellar spectra and raw and detrended white light curves for each visit are shown in Figure 3.

We marginalized over the entire set of functions following the framework outlined in Gibson (2014). Marginalization over multiple systematics models assumes equally weighted priors for each model tested. Table 8 shows the results for each systematics model using the STIS white light curves. The reduced chi-squared χ_r from the fits can be used as a proxy for the photon noise level of a given data set (Nikolov et al. 2014). We selected the systematics model for use in detrending the STIS white light curves based on the lowest AIC value because the light curves show no significant correlation to the quantified systematic parameters (Nikolov et al. 2014).

4.2. STIS Spectrophotometric Light Curves

We produced the spectrophotometric light curves by dividing the spectra into bins of width 17–400 Å and integrating the flux from each bandpass. The width of the bins is determined primarily by the need to achieve a given photometric precision to be sensitive to features in the planet's transmission spectrum that are comparable in amplitude to an atmospheric scale height. The smaller bin sizes were chosen to be centered at specific absorption features, such as Na I at 5893 Å and K I at 7665 Å.

We modeled the systematic errors using two methods. In the first approach, we independently fit each of the binned light curves with the same family of transit+systematics models (see Appendix B.1) as the broadband light curve. The only differences are that we fixed the midtransit time T_0 and the scaled semimajor axis $a/R_\star$ to the white light curve best-fit values. We also fixed the limb-darkening coefficients (computed following the procedure outlined in Section 4.4) to the derived theoretical values. In the second approach, we performed a common mode correction to remove color-independent systematic trends from each spectral bin. Then, we fit the common-mode-corrected spectroscopic light curves by fitting for residuals with a parameterized model of six fewer free parameters ($c_1 - c_4$, T_0, and $a/R_\star$) and marginalizing over the entire set of functions defined in Appendix B.1. The common mode trends are computed by dividing the raw flux of the white light curve in each grating by the best-fit analytic transit model. We applied the common mode correction by dividing each binned light curve by the derived common-mode flux. Removing common mode trends is known to reduce the amplitude of the observed *HST* breathing systematics, since these trends are similar in wavelength across the detector (Sing et al. 2013; Nikolov et al. 2014). The common-mode-corrected light curves are shown in Figure 3.

Both methods produced similar results (i.e., consistent baseline in $R_p/R_\star$). Since the common mode correction produces lower dispersion in the spectrophotometric light curves and smaller $R_p/R_\star$ uncertainties (Nikolov et al. 2015), we report the common-mode-corrected results for the fitted $R_p/R_\star$ (before and after applying the correction for unocculted spots discussed in Section 3.4) and nonlinear limb-darkening coefficients for each spectroscopic channel in Table 5. The raw and detrended STIS spectrophotometric light curves for the G430L and G750L gratings are shown in Figures 4–6.

4.3. IRAC Light Curves

We modeled the 3.6 and 4.5 μm IRAC transit photometry in accordance with the methods outlined in Sing et al. (2011b, 2013) and Nikolov et al. (2014). To correct for flux variations from intrapixel sensitivity, we fit a polynomial to the stellar centroid position (Charbonneau et al. 2005, 2008; Reach et al. 2005; Knutson et al. 2008). This technique is effective on short timescales (<10 hr) and for small (<0.2 pixels) variations in the stellar centroid position (Lewis et al. 2013). We corrected

Table 5
Broadband Transmission Spectrum Results for WASP-52b for the STIS G430L and G750L and *Spitzer* IRAC Data

λ (Å)	$(R_p/R_*)_{\rm uncorr}$	$(R_p/R_*)_{\rm corr}$	c_1	c_2	c_3	c_4
2900–3700	0.16957 ± 0.00385	0.15421 ± 0.00677	0.4371	−0.7679	1.6319	−0.3645
3700–3950	0.16684 ± 0.00201	0.15781 ± 0.00296	0.7648	−1.1573	1.7190	−0.4157
3950–4113	0.16703 ± 0.00157	0.16681 ± 0.00296	0.4778	−0.6459	1.6564	−0.5511
4113–4250	0.16871 ± 0.00102	0.16457 ± 0.00159	0.4831	−0.6750	1.7025	−0.5879
4250–4400	0.16672 ± 0.00116	0.16394 ± 0.00148	0.6151	−0.8347	1.7798	−0.6519
4400–4500	0.16618 ± 0.00112	0.16101 ± 0.00142	0.4691	−0.4858	1.5912	−0.6570
4500–4600	0.16685 ± 0.00113	0.16358 ± 0.00149	0.4777	−0.4094	1.5029	−0.6494
4600–4700	0.16827 ± 0.00089	0.16583 ± 0.00106	0.5977	−0.6932	1.6924	−0.6811
4700–4800	0.16625 ± 0.00120	0.16211 ± 0.00187	0.4411	−0.2389	1.1548	−0.4505
4800–4900	0.16630 ± 0.00088	0.16290 ± 0.00115	0.5159	−0.3136	1.2538	−0.5560
4900–5000	0.16557 ± 0.00119	0.16079 ± 0.00156	0.4399	−0.1314	1.0138	−0.4335
5000–5100	0.16806 ± 0.00085	0.16463 ± 0.00105	0.5409	−0.3989	1.1899	−0.4566
5100–5200	0.16888 ± 0.00120	0.16623 ± 0.00175	0.5605	−0.4363	1.0910	−0.3757
5200–5300	0.16769 ± 0.00074	0.16541 ± 0.00103	0.5381	−0.2913	1.0934	−0.4736
5300–5400	0.16589 ± 0.00101	0.16330 ± 0.00114	0.5732	−0.3581	1.1751	−0.5264
5400–5500	0.16802 ± 0.00091	0.16416 ± 0.00132	0.5975	−0.4018	1.1388	−0.4758
5500–5600	0.16665 ± 0.00083	0.16279 ± 0.00108	0.6370	−0.4886	1.2206	−0.5147
5600–5700	0.16621 ± 0.00086	0.16157 ± 0.00154	0.5662	−0.2476	0.9413	−0.4076
5700–5800	0.16782 ± 0.00172	0.16566 ± 0.00170	0.5828	−0.2962	1.0423	−0.4802
5800–5878	0.16556 ± 0.00195	0.16346 ± 0.00192	0.6127	−0.3245	0.9821	−0.4278
5878–5913	0.17087 ± 0.00209	0.16858 ± 0.00206	0.6511	−0.5383	1.2452	−0.5387
5913–6070	0.16643 ± 0.00112	0.16434 ± 0.00110	0.6208	−0.3332	0.9989	−0.4502
6070–6200	0.16515 ± 0.00105	0.16310 ± 0.00105	0.6192	−0.3316	0.9650	−0.4310
6200–6300	0.16611 ± 0.00160	0.16407 ± 0.00157	0.6439	−0.3583	0.9653	−0.4321
6300–6450	0.16590 ± 0.00095	0.16388 ± 0.00094	0.6508	−0.3875	0.9927	−0.4467
6450–6600	0.16371 ± 0.00087	0.16179 ± 0.00086	0.6569	−0.3766	0.9577	−0.4418
6600–6800	0.16633 ± 0.00103	0.16439 ± 0.00102	0.6561	−0.3747	0.9214	−0.4106
6800–7000	0.16419 ± 0.00170	0.16231 ± 0.00168	0.6494	−0.3485	0.8652	−0.3871
7000–7200	0.16491 ± 0.00091	0.16307 ± 0.00090	0.6824	−0.4389	0.9298	−0.4051
7200–7450	0.16448 ± 0.00068	0.16268 ± 0.00067	0.6914	−0.4691	0.9457	−0.4158
7450–7645	0.16656 ± 0.00126	0.16479 ± 0.00126	0.6972	−0.4678	0.9219	−0.4080
7645–7720	0.16113 ± 0.00312	0.15943 ± 0.00309	0.7151	−0.5133	0.9350	−0.4061
7720–8100	0.16805 ± 0.00121	0.16632 ± 0.00121	0.6976	−0.4689	0.8838	−0.3862
8100–8485	0.16538 ± 0.00081	0.16372 ± 0.00080	0.7008	−0.4971	0.8888	−0.3849
8485–8985	0.16572 ± 0.00096	0.16413 ± 0.00095	0.7212	−0.5332	0.8718	−0.3765
8985–10300	0.16607 ± 0.00089	0.16459 ± 0.00088	0.7134	−0.5378	0.8618	−0.3737
36000	0.16305 ± 0.00050	0.16305 ± 0.00050	0.4935	−0.2505	0.1831	−0.0638
45000	0.16390 ± 0.00110	0.16390 ± 0.00110	0.5344	−0.5777	0.5534	−0.1991

for systematic effects using a model given by the linear combination

$$f(t) = a_0 + a_1 x + a_2 x^2 + a_3 y + a_4 y^2 + a_5 xy + a_6 t, \quad (3)$$

where $f(t)$ is the stellar flux as a function of time, the coefficients a_0 through a_6 are free fitting parameters, x and y are the detector positions of the stellar centroid, and t is time. We generate all possible model combinations of Equation (3), which we marginalize over using the Gibson (2014) procedure as detailed in Section 4.1 and Appendix B.1. Using the WASP-52 system parameters from Hébrard et al. (2013) as priors, we jointly fit for all parameters and find that our results (see Table 4) agree within 1σ with the STIS white light curve analysis. To measure $R_p/R_\star$ for the transmission spectrum, we fixed the orbital period P, normalized planet semimajor axis $a/R_\star$, inclination i, and central transit time T_0 to the best-fit values from the joint fit. The limb-darkening coefficients were also fixed to their theoretical values based on 3D stellar atmosphere models (see Section 4.4). The measured planetary radius and limb-darkening coefficients are included in Table 5. Figures 7 and 8 show the raw and detrended *Spitzer* transit light curves.

4.4. Limb-darkening Models

We modeled the limb darkening of WASP-52b using the four-parameter nonlinear limb-darkening law (Claret 2000) given by

$$\frac{I(\mu)}{I(1)} = 1 - \sum_{n=1}^{4} c_n (1 - \mu^{n/2}), \quad (4)$$

where $I(1)$ is the intensity at the center of the stellar disk, c_n (n = 1–4) are the limb-darkening coefficients, and $\mu = \cos(\theta)$, where θ is the angle between the normal to the stellar surface and the line of sight.

To derive the stellar limb-darkening coefficients, we followed the procedure described in Sing (2010) and initially used values for the four limb-darkening coefficients based on 1D ATLAS theoretical stellar models (Kurucz 1993). We then derived the limb-darkening coefficients from 3D stellar models (Magic et al. 2015) and compared to the 1D results to eliminate the known wavelength-dependent degeneracy of limb

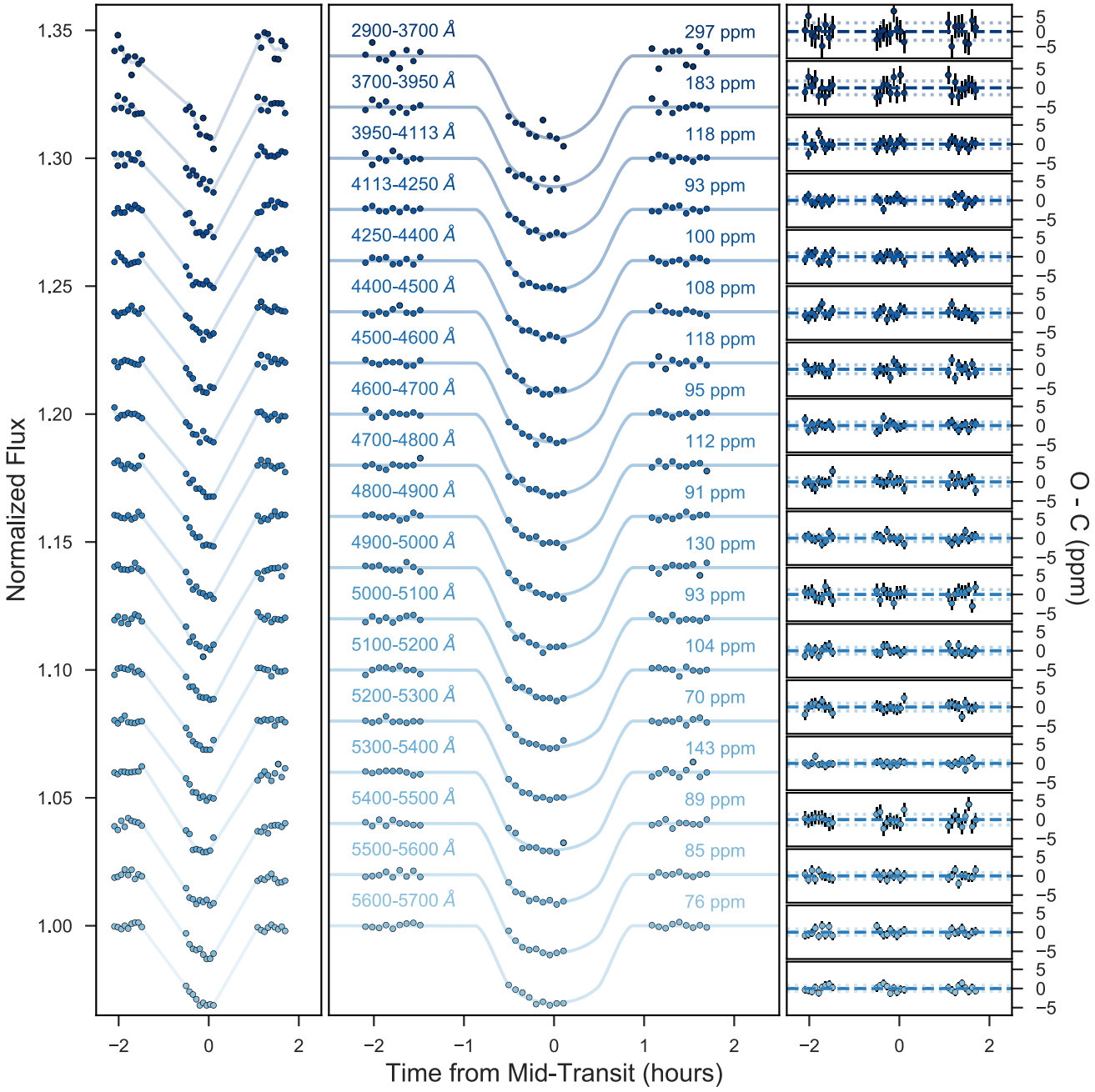

Figure 4. *HST*/STIS G430L observations of WASP-52b visit 52, excluding the first orbit and the first exposure of each subsequent orbit. Raw (left panel) and detrended (middle panel) light curves are shown for each wavelength bin and are offset vertically by an arbitrary constant for clarity. Observed minus computed residuals with error bars are shown in the right panel.

darkening with transit depth (Sing et al. 2008a). This approach reduces the number of free parameters in the fit (typically four parameters per grating), but may cause an underestimation of errors in the derived spectrum. The derived nonlinear 3D limb-darkening coefficients for each spectrophotometric light curve are shown in Table 5.

5. Results

The broadband STIS+*Spitzer* transmission spectrum for WASP-52b corrected for stellar activity and compared to theoretical forward atmospheric models (Goyal et al. 2018) and past transmission spectrum measurements (Chen et al. 2017; Louden et al. 2017) is shown in Figure 9. The transmission spectrum shows evidence of Na I absorption (5893 Å) at 2.3σ confidence and no observable detection of K I absorption. To visualize the amplitude of the spot corrections, we also compare the raw transmission spectrum (before applying the stellar activity correction) and the spot-corrected spectrum in Figure 10.

5.1. Constraints on Na I and K I

We inspect the presence and significance of the Na I and K I features in the WASP-52b transmission spectrum using a grid of spectrophotometric channels ranging in width from 30 to 255 Å in steps of 15 Å, centered on the Na I (5893 Å) and K I (7665 Å) resonance doublets. The minimum bin size (30 Å) is

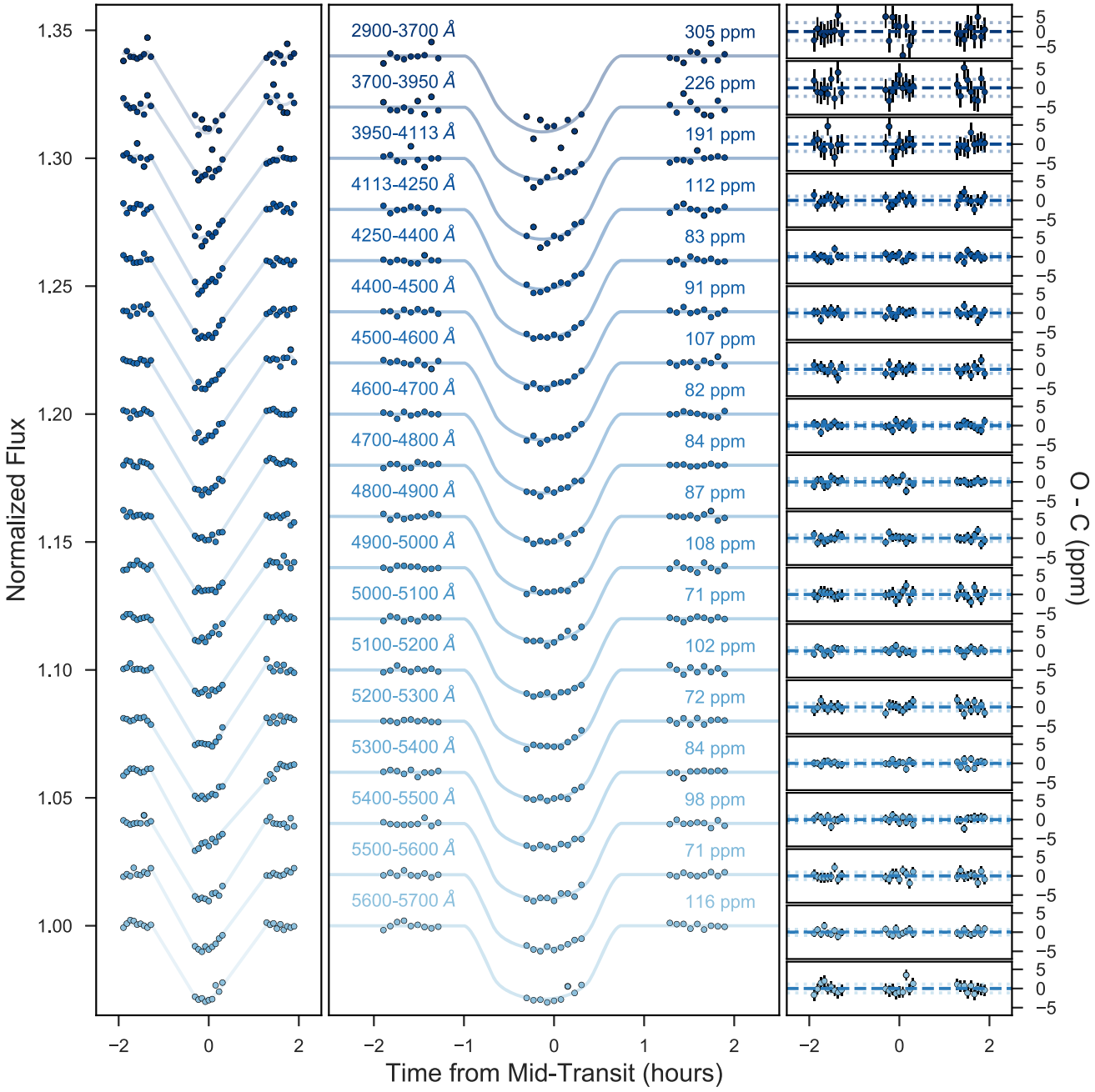

Figure 5. Same as Figure 4, but for visit 53.

defined to include both doublet lines. If a planetary atmospheric signal is present, this binning scheme should demonstrate a gradual decay in the measured transit depth for larger bin sizes. The results of this analysis are shown in Figure 11.

For the Na I feature, we note a gradual decrease in the measured transit depth for bins 30–100 Å wide. For wider bins, the signal is largely washed out and the transit depth remains unchanged within the uncertainties. This trend is expected when observing a narrow absorption peak and is consistent with the presence of a cloud deck. By measuring the difference in transit depth between the narrowest (30 Å) bin and the flat transit depth baseline, we detect the core of the Na I doublet at 2.3σ confidence. In the case of K I, we do not see evidence of absorption even in the narrowest spectroscopic channel, suggesting that this feature is either masked by a thick cloud deck or not as abundant in the atmosphere of WASP-52b. For further discussion, see Section 6.1.

5.2. Fits to Forward Atmospheric Models

We fit the combined STIS+*Spitzer* transmission spectrum to the publicly available grid of forward model transmission spectra (Goyal et al. 2018) produced using the ATMO 1D radiative–convective equilibrium model (Amundsen et al. 2014; Tremblin et al. 2015, 2016; Drummond et al. 2016). The models are generated for the parameters (e.g., mass, radius, gravity) of WASP-52b.

The grid[19] includes 3920 model transmission spectra of WASP-52b for five temperatures (1015, 1165, 1315, 1465,

[19] https://bd-server.astro.ex.ac.uk/exoplanets/WASP-52/

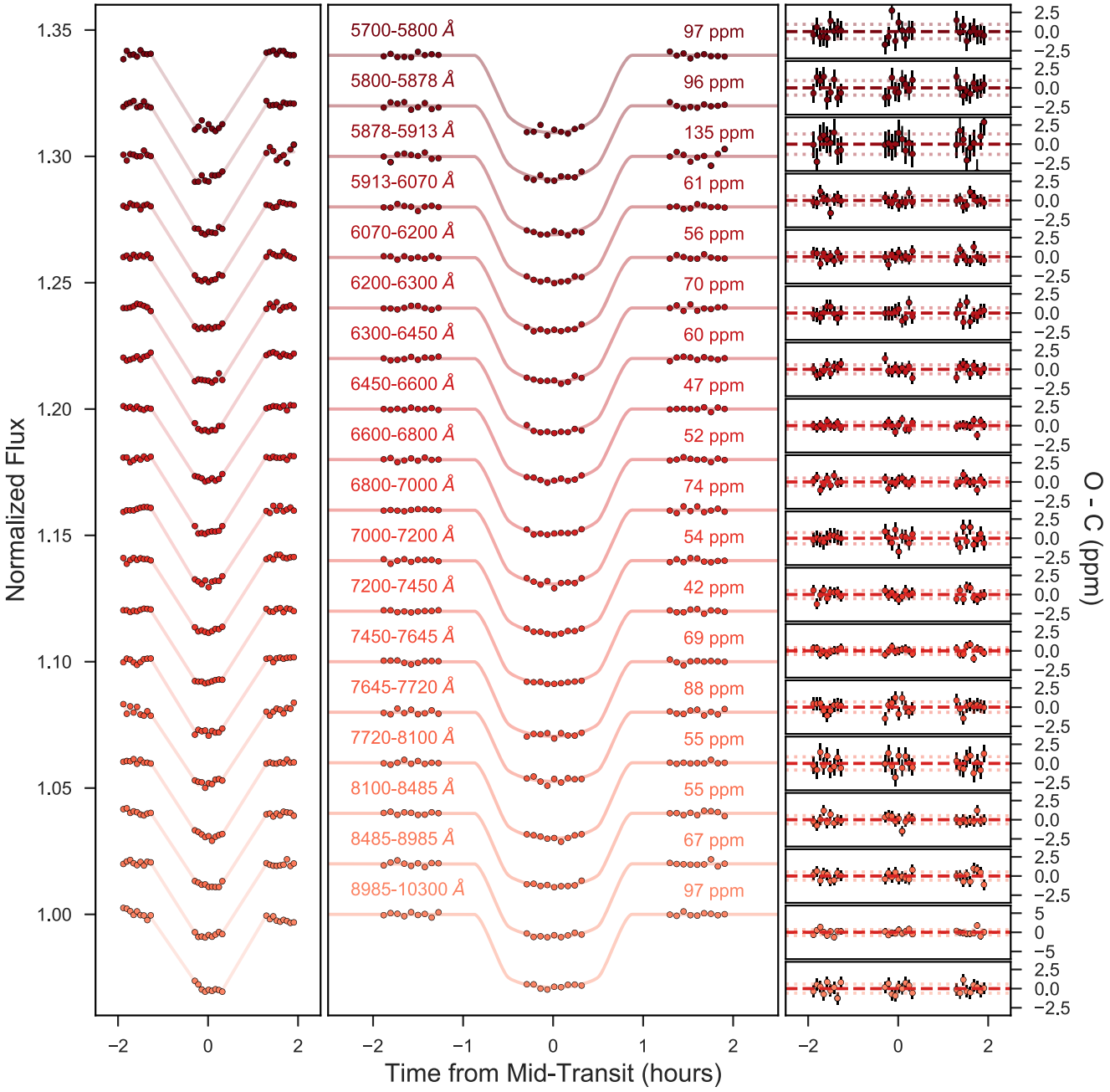

Figure 6. *HST*/STIS G750L observations of WASP-52b visit 54, excluding the first orbit and the first exposure of each subsequent orbit. Raw (left panel) and detrended (middle panel) light curves are shown for each wavelength bin and are offset vertically by an arbitrary constant for clarity. Observed minus computed residuals with error bars are shown in the right panel.

1615 K), seven metallicities (0.005, 0.1, 1, 10, 50, 100, 200× solar), seven C/O ratios (0.15, 0.35, 0.56, 0.70, 0.75, 1.0, and 1.5), four values of the haziness parameter $\alpha_{\rm haze}$ (1, 10, 150, and 1100), and four values of the cloudiness parameter $\alpha_{\rm cloud}$ (0, 0.06, 0.2, and 1). The parameter $\alpha_{\rm haze}$ is a proxy for the haze enhancement factor of small scattering aerosol particles suspended in the atmosphere, where $\alpha_{\rm haze} = 1$ indicates no haze and $\alpha_{\rm haze} = 1100$ indicates thick hazes. The cloudiness parameter $\alpha_{\rm cloud}$ gives the strength of gray scattering due to H_2 at 350 nm, with $\alpha_{\rm cloud} = 0$ corresponding to no clouds and $\alpha_{\rm cloud} = 1$ corresponding to a thick cloud deck. See Goyal et al. (2018) and references therein for further details. The transmission spectra are computed assuming isothermal pressure−temperature ($P - T$) profiles and condensation without rainout (local condensation).

We computed the mean model prediction for the wavelength range of each spectroscopic channel (see Table 5) and performed a least-squares fitting of the band-averaged model to the spectrum. For the fitting procedure, we allowed the vertical offset in $R_p/R_\star$ between the spectrum and model to vary while holding all other parameters fixed in order to preserve the model shape. The number of degrees of freedom for each model is $n - m$, where n is the number of data points and m is the number of fitted parameters. Since $n = 38$ and $m = 1$, the number of

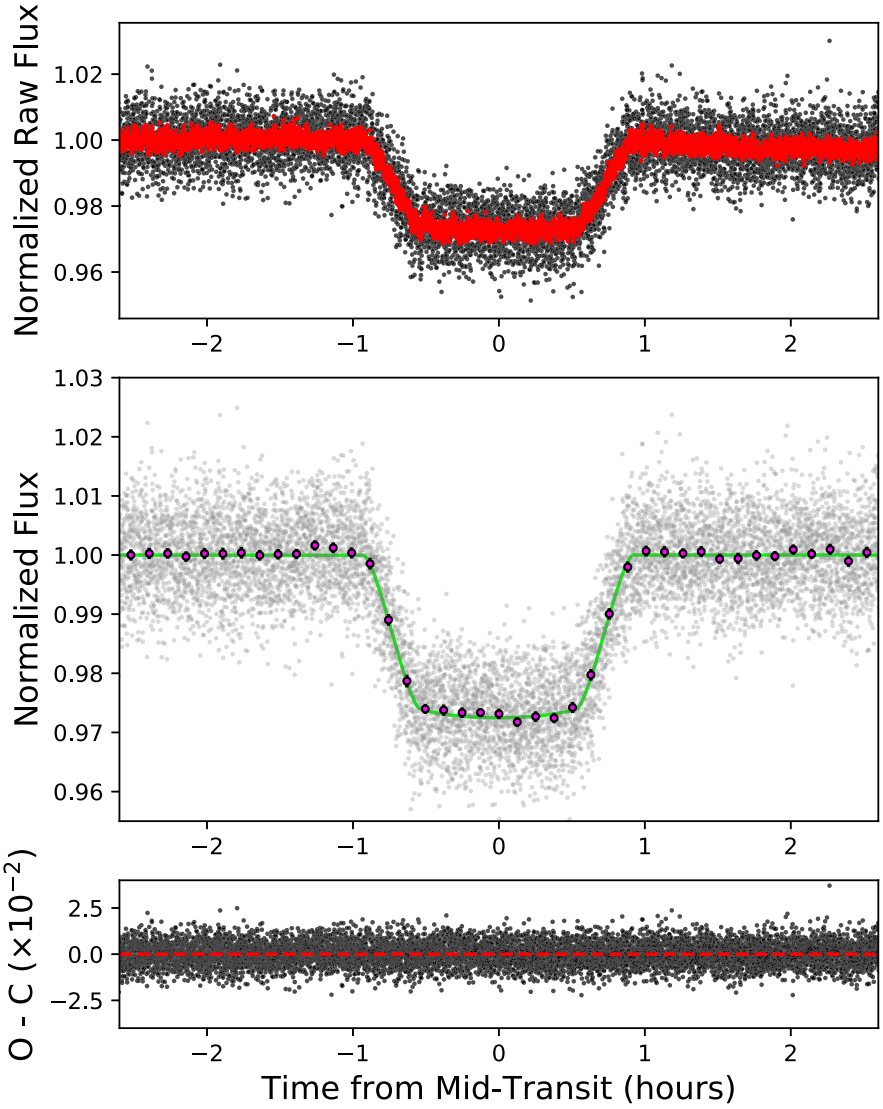

Figure 7. *Spitzer*/IRAC 3.6 μm transit light curve. Top panel: raw flux (black points) and best-fit transit model (red points). Middle panel: detrended light curve (gray points) and best-fit transit model (green line) overlaid with the binned light curve (magenta points; 45 bins of 224 data points each). Bottom panel: observed minus computed residuals (black points) of the raw light curve.

degrees of freedom for each model is constant. From the fits, we computed the χ^2 statistic to quantify our model selection.

Figure 9 shows the best-fit model, representative clear and hazy models, and a flat model compared to the observed transmission spectrum. The best-fitting model ($\chi^2 = 39.3$) is cloudy ($\alpha_{\rm cloud} = 1.0$) and slightly hazy ($\alpha_{\rm haze} = 10$) with a 2.3σ signature of Na I absorption, a temperature of $T = 1315$ K, solar metallicity ([M/H] = 0.0), and slightly supersolar C/O (C/O = 0.70). The selected clear model ($\chi^2 = 49.5$) has a lower temperature ($T = 1015$ K) and no clouds ($\alpha_{\rm cloud} = 0.00$) or hazes ($\alpha_{\rm haze} = 1$). The representative hazy model ($\chi^2 = 43.3$) is similar to the clear model, but with extreme haziness ($\alpha_{\rm haze} = 1100$). The flat model ($\chi^2 = 52.2$) represents a featureless (gray) spectrum.

The χ^2 contour plot for the model grid fits is shown in Figure 12. The grid provides constraints on the atmospheric and physical parameters of WASP-52b, with the 1σ confidence region favoring high cloudiness, slight haziness, solar metallicity, slightly supersolar C/O ratio (>0.56), and an equilibrium temperature of 1315 K.

5.3. Comparison with Previous Results

In addition to the combined STIS+*Spitzer* transmission spectrum we report here, there are two ground-based optical transmission spectrum measurements for WASP-52b. Most recently, Louden et al. (2017) used spectroscopy between 4000 and 8750 Å for two transit observations from the ACAM instrument mounted on the William Herschel Telescope (WHT). Chen et al. (2017) observed one transit with the Gran Telescopio Canarias's (GTC) OSIRIS instrument in the 5220–9030 Å wavelength range. We show these transmission spectra compared to our STIS+*Spitzer* results in Figure 9.

With the WHT/ACAM observations, Louden et al. (2017) modeled spot-crossing events via GPs, adopted a harmonic analysis of ground-based photometric monitoring, and found varying levels of activity over time with evidence of differential rotation. These results reveal a flat transmission spectrum attributed to an optically thick cloud deck. The GTC/OSIRIS observations indicate a cloudy atmosphere with a $\sim 3\sigma$ detection of Na I and a weaker detection of K I. Calculations of the integrated absorption depth for the Na I and K I signals

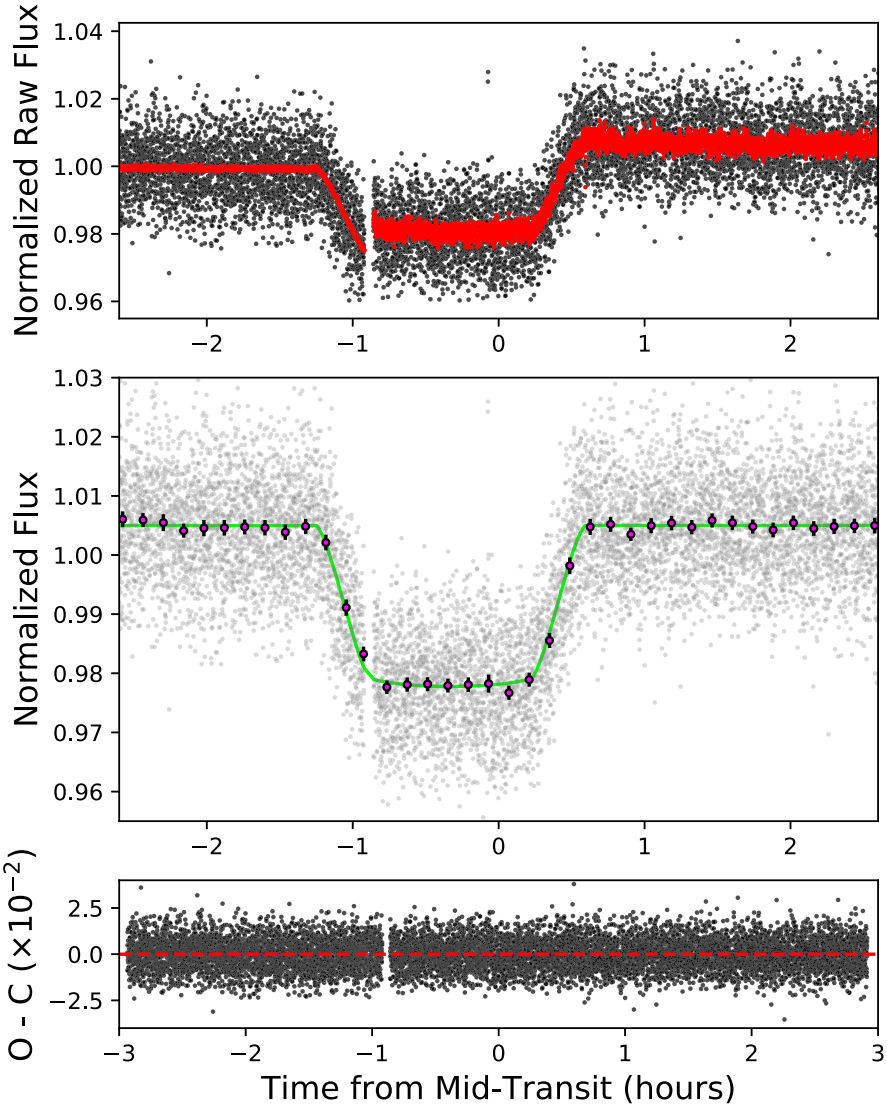

Figure 8. *Spitzer*/IRAC 4.5 μm transit light curve. Top panel: raw flux (black points) and best-fit transit model (red points). The small gap at the end of the transit ingress corresponds to the delay between subsequent data readouts. Middle panel: detrended light curve (gray points) and best-fit transit model (green line) overlaid with the binned light curve (magenta points; 43 bins of 239 data points each). Bottom panel: observed minus computed residuals (black points) of the raw light curve.

suggest an inverted temperature structure for the upper atmosphere of WASP-52b (Chen et al. 2017).

Our $R_p/R_\star$ baseline is consistent within 1σ with the ground-based transmission spectrum from WHT/ACAM (Louden et al. 2017). The most significant difference is that the WHT spectrum does not show any variation in $R_p/R_\star$ around 5893 Å. If there is a weak signal of Na I absorption from the planet, the resolution of the spectrum, composed of equally sized spectrophotometric bins of width 250 Å, may be washing it out, as illustrated in Figure 11.

The baseline of our spectrum matches less well with the ground-based GTC/OSIRIS transmission spectrum (Chen et al. 2017). We note a constant offset in the absolute measured transit depths of our STIS+*Spitzer* spectrum and the GTC measurement, with a difference in the $R_p/R_\star$ baseline of $\sim 3\sigma$. The authors attribute their shallower transit depth measurement compared to previous studies (e.g., Hébrard et al. 2013; Kirk et al. 2016; Mancini et al. 2017) to the effects of stellar activity. We find evidence of a Na I signal that is consistent with the GTC detection within 1σ, but our spectrum shows no evidence of K I absorption, contrary to the Chen et al. (2017) result. This discrepancy could be due to the different methods used to correct for the effects of stellar activity (see Section 3 and see Chen et al. 2017).

5.4. Comparison to HAT-P-1b

We compared WASP-52b to the well-studied inflated hot Jupiter HAT-P-1b (see Nikolov et al. 2014) because both planets have comparable system parameters and atmospheric properties. HAT-P-1b and WASP-52b have overlapping surface gravity, equilibrium temperature, mass, radius, and stellar irradiation, and the transmission spectra of both planets are marginally flat with evidence of Na I absorption but no observable K I absorption. Table 6 compares the stellar and planetary parameters for WASP-52 (Hébrard et al. 2013; Table 4) and HAT-P-1 (Nikolov et al. 2014).

HAT-P-1b has a precise transmission spectrum measurement from *HST*/STIS (Nikolov et al. 2014), which we use to compare the atmospheric properties of both planets. For this comparison, we reconstructed the *HST*/STIS transmission spectrum for WASP-52b using the same binning scheme of

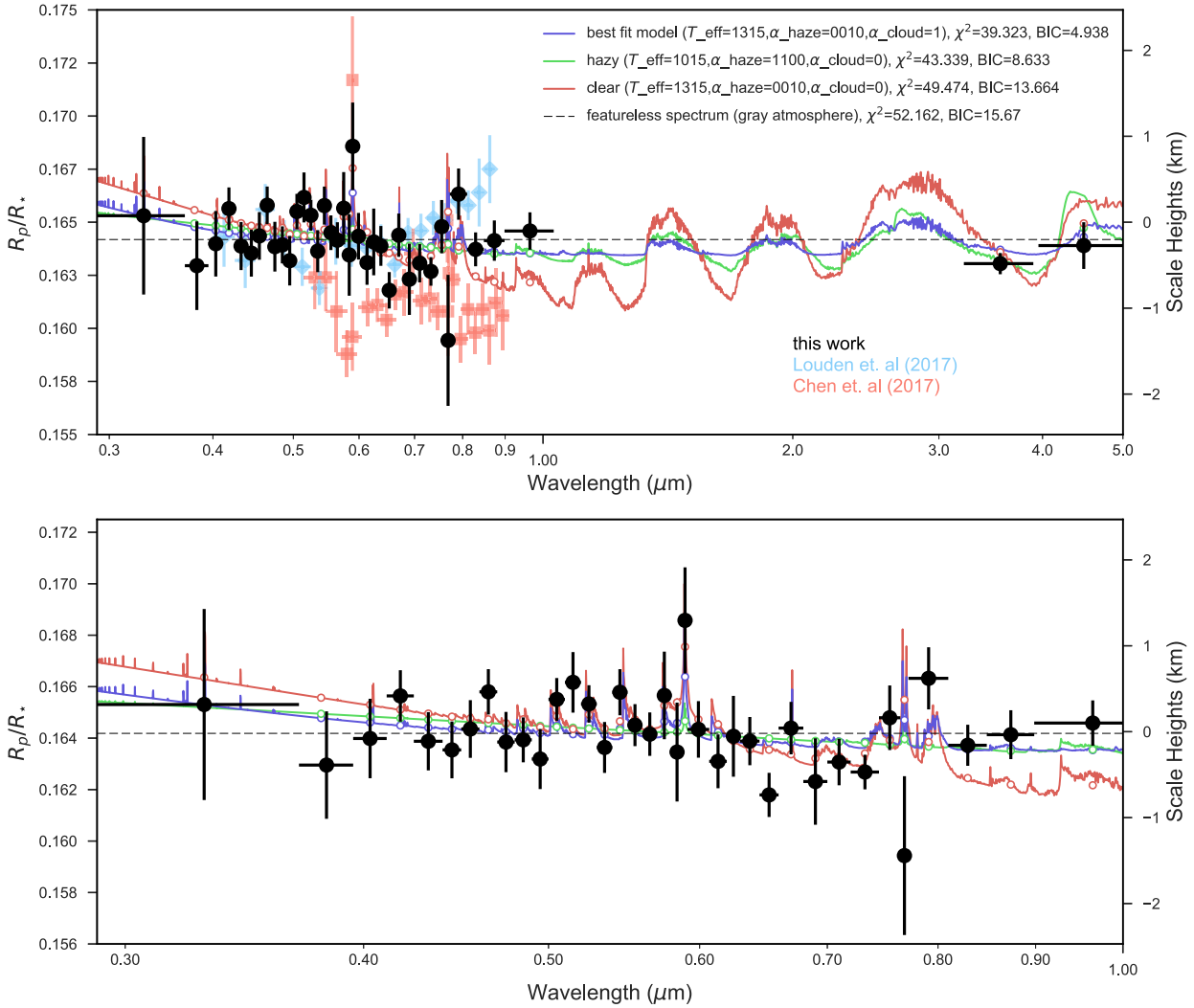

Figure 9. Top panel: transmission spectrum corrected for stellar activity for WASP-52b from *HST*/STIS and *Spitzer*/IRAC (black circles). Ground-based optical transmission spectrum measurements from Louden et al. (2017; blue diamonds) and Chen et al. (2017; salmon rectangles) are included for comparison. We show a subset of the best-fit theoretical atmospheric models (lines), and we find that the observed transmission spectrum is consistent with evidence of Na I at 2.3σ confidence and a cloudy atmosphere with no TiO. Models are smoothed by a constant. The average $R_p/R_\star$ baseline of the transmission spectrum (dashed black line) is shown for reference. Bottom panel: same as above, but zoomed in to the STIS wavelength range (~0.29–1.0 μm).

Nikolov et al. (2014) for HAT-P-1b and fit the light curves for these bins based on the methods outlined in Section 4. Figure 13 shows the *HST*/STIS transmission spectra of both planets with identical binning. Based on this comparison, the spectra of both planets are identical within the uncertainties with an average 1σ difference.

As reported in Nikolov et al. (2014), the best-fit model for HAT-P-1b is a hazy spectrum with Na I absorption and an extra optical absorber to account for the observed absorption enhancement at wavelengths longer than ~0.85 μm. To directly compare this interpretation to the WASP-52b results reported here, we fit the HAT-P-1b spectrum (Nikolov et al. 2014) to the open source ATMO grid of forward models generated for the parameters of HAT-P-1b (see Appendix C and Figure 16 for details). The best-fit model parameters for HAT-P-1b and WASP-52b are shown in Table 6.

Since WASP-52b and HAT-P-1b have similar optical transmission spectra (~0.29–1 μm), we compare the atmospheric properties of these planets in the near-infrared to ascertain if these planets would be good candidates for comparative atmospheric analyses with *JWST*. Figure 14 shows the best-fit models for both planets from 0.29 to 5 μm. Beyond 1 μm, we find that the best-fitting models for HAT-P-1b and WASP-52b do not agree with each other as they do in the optical. For further discussion regarding potential reasons for this near-infrared discrepancy, see Section 6.2.

6. Discussion

6.1. Interpreting Alkali Detections in the Presence of Clouds

As reported in Section 5.1, we find hints of Na I absorption but no evidence of K I in the transmission spectrum of WASP-52b. A similar trend has been observed for HD 189733b (Pont et al. 2013), HAT-P-1b (Nikolov et al. 2014), and WASP-17b (Sing et al. 2016). The reverse trend (i.e., the presence of a K I signal but no Na I) has been observed in several planets, including WASP-31b (Sing et al. 2015) and HAT-P-12b (Sing et al. 2016). We note, however, that the majority of current sodium and potassium detections in exoplanet atmospheres are low significance, and a nondetection of K I can only be interpreted as an

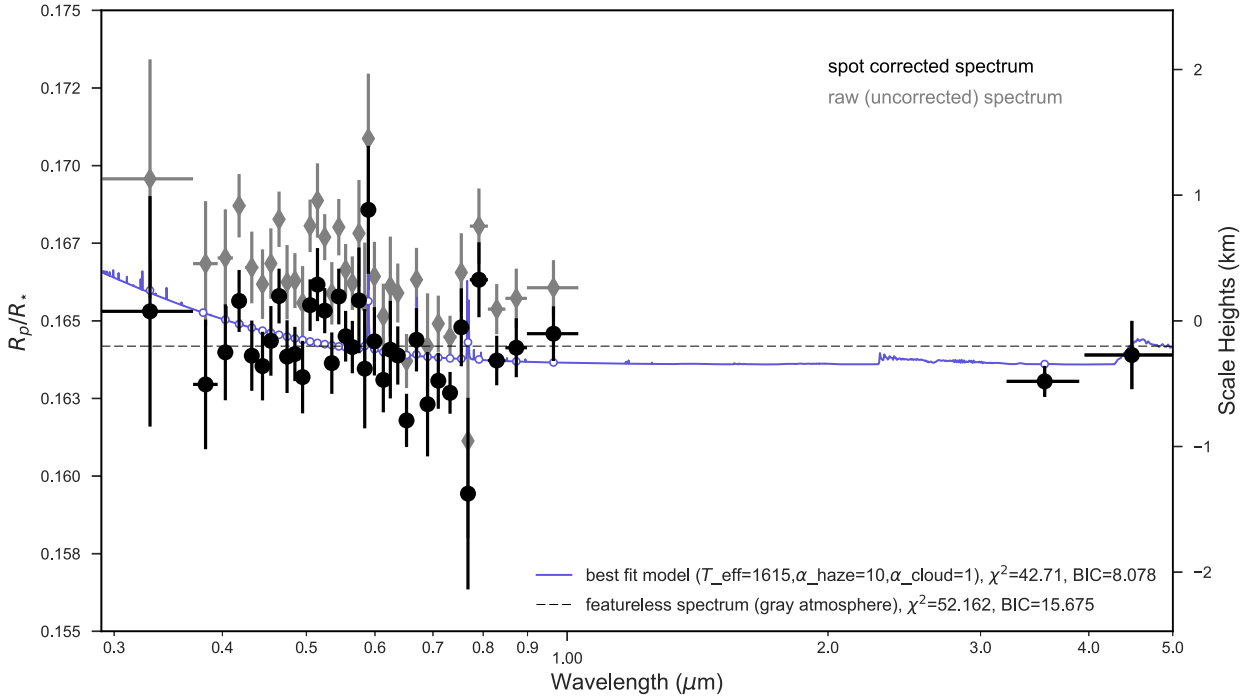

Figure 10. Comparison of the raw (gray diamonds) and spot-corrected (black circles) transmission spectra for WASP-52b. The best-fitting (solid blue line) and gray atmosphere (dashed black line) models from Figure 9 are shown for reference.

upper limit to the abundance of that element in the atmospheric layers probed by our observations, considering their uncertainties. Based on the available data and their uncertainties, we estimate an abundance ratio of $\ln[\mathrm{Na}/\mathrm{K}] = 8.32^{+6.51}_{-6.03}$. This value is consistent with solar abundances but has large uncertainties and is not well constrained.

These results are consistent with our forward model analysis, which favors the presence of clouds and slight hazes that mute spectroscopic features in the planet's atmosphere. The best-fitting models give temperatures in the range $T \sim 1000$–1300 K. Compared to the planet's equilibrium temperature ($T_{\rm eq} = 1315$ K; Hébrard et al. 2013), these temperature estimates may be driven by the gradient of the Rayleigh scattering slope. Significant sodium condensation in the form of Na_2S is expected at lower temperatures (~1000 K) and potassium condensation in the form of KCl at even lower temperatures (~600 K; Marley et al. 2013). Tenuous Na_2S and KCl clouds could form at shallow pressures in WASP-52b's atmosphere, since the equilibrium temperature does not represent the full range of temperatures in a planet's atmosphere. The cloud deck in WASP-52b's atmosphere could therefore be composed of species other than sodium or potassium compounds, such as silicates.

Regardless of the composition of these clouds, they are likely masking the K I feature and the wings of the Na I resonance core. We do not resolve the broad wings of the Na I line (Figure 11), which may suggest the presence of an extra absorber or scatterer in the atmosphere that is obscuring or masking the atmospheric Na I and K I absorption features (Seager & Sasselov 2000; Nikolov et al. 2014).

If a K I signal is truly lacking in the transmission spectrum of WASP-52b, an alternative explanation could be attributed to an underabundance of this element in the planetary atmosphere. If the cloud deck is composed of sodium or potassium compounds, however, the gas-phase abundances of these species would not reflect primordial abundances. Since K I is a weaker spectroscopic feature, it may be present in the planet's atmosphere but not detectable with the precision of the STIS data. Higher resolution, higher precision observations are necessary to confirm this idea.

6.2. Contextualizing WASP-52b

Although the atmospheres of planets studied thus far appear diverse (Sing et al. 2016), we have not yet been able to identify any clear correlations between planetary atmospheric properties and other system parameters. Comparing the transmission spectra of planets with similar system parameters may therefore prove insightful in searching for common atmospheric characteristics. WASP-52b is a good target for such comparisons because the well-studied inflated hot Jupiter HAT-P-1b has comparable system parameters and atmospheric properties.

We compare the observed transmission spectrum of WASP-52b presented here to that of the well-studied inflated hot Jupiter HAT-P-1b. These two planets have similar system parameters (see Table 6), although WASP-52 is ~0.9 times more active than HAT-P-1b (Nikolov et al. 2014). Additionally, the optical transmission spectra of both planets are marginally flat with evidence of Na I but no observable evidence of K I. We compare their transmission spectra with identical binning schemes in Figure 13, and we find that the spectra of both planets in the optical (~0.29–1 μm) are identical within the uncertainties with an average 1σ difference.

Extending this comparison to near-infrared wavelengths, however, reveals that their transmission spectra differ considerably beyond 1 μm. The best-fit ATMO model for WASP-52b shows muted H_2O and CH_4 spectral features compared to the best-fitting HAT-P-1b model, which could indicate that WASP-52b has a higher aerosol layer. Near-infrared *HST*/WFC3 observations of HAT-P-1b reveal H_2O absorption at $>5\sigma$ confidence (Wakeford et al. 2013), and the deep H_2O

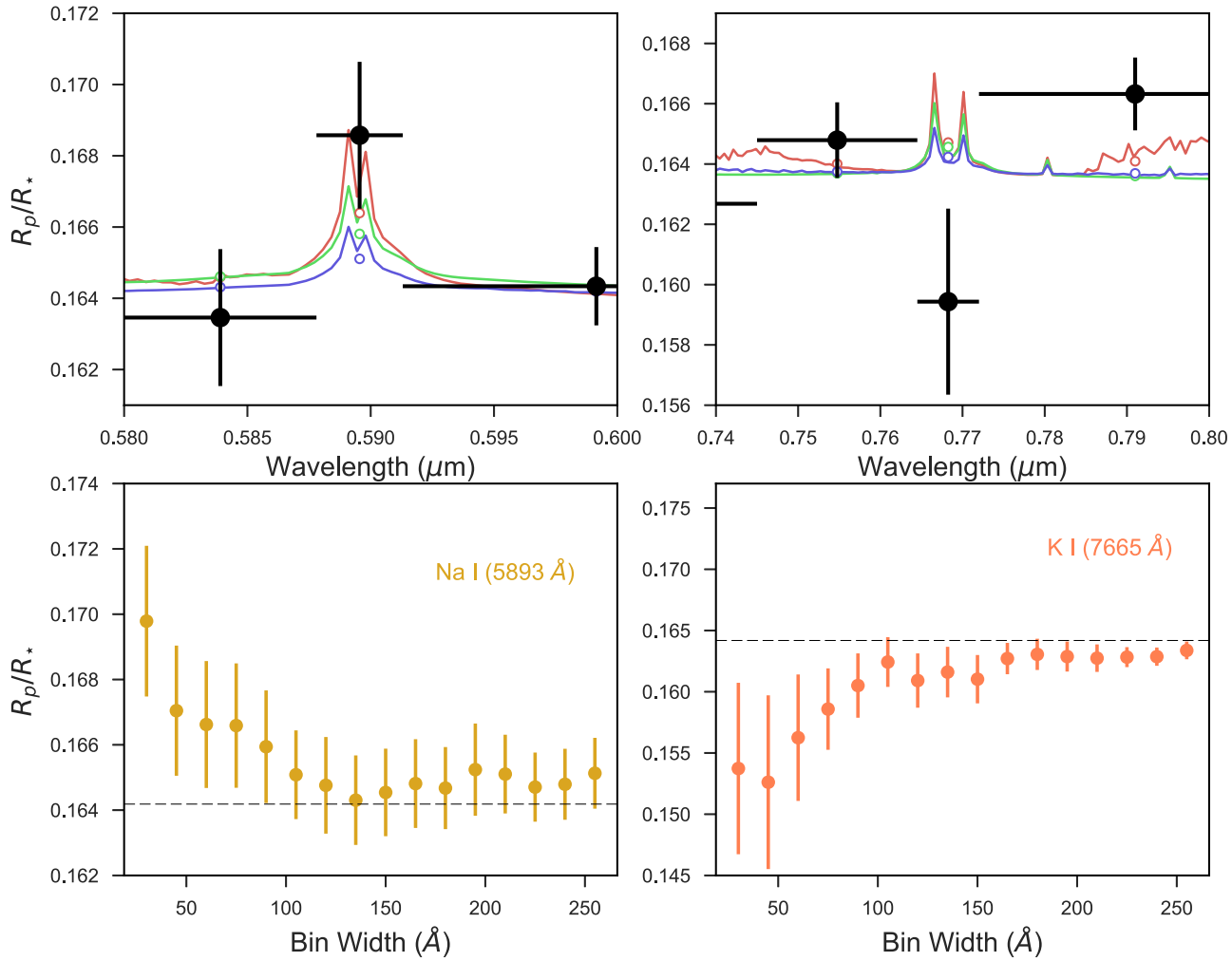

Figure 11. Top panel: WASP-52b transmission spectrum (black points) zoomed in to the central wavelength of Na I at 5893 Å (left) and K I at 7665 Å (right) with the best-fit (blue), hazy (green), and clear (red) models overplotted. Bottom panel: absorption depth of Na I at 5893 Å (left) and K I at 7665 Å (right) for spectroscopic channels ranging in size from 30 to 255 Å. The average $R_p/R_\star$ baseline of the transmission spectrum (dashed black line) is shown for reference.

feature shown in the best-fit ATMO model matches these data. The best-fit atmospheric model for WASP-52b shows a weaker (but still observable) H_2O feature at 1.4 μm, and evidence of H_2O absorption at 1.4 μm for WASP-52b has recently been shown in Bruno et al. (2018). The activity levels of the host stars may also contribute to the divergence of the transmission spectra for these two planets at near-infrared wavelengths, although observations of the stellar UV fluxes are necessary to confirm this hypothesis. Comparative near-infrared observations with *JWST* can confirm the atmospheric similarities of these planets at shallower atmospheric layers compared to those probed by STIS.

7. Summary

Our key results are summarized as follows:

1. We present an optical to near-infrared transmission spectrum of WASP-52b (measured to a median precision of 90 ppm) from ~0.29 to 5.0 μm using transit observations from *HST*/STIS and *Spitzer*/IRAC. We correct for the effects of stellar activity and fit the observed transmission spectrum to a grid of forward atmospheric models.
2. Based on these fits (Figure 9), we find that our transmission spectrum measurement best matches a moderately cloudy atmospheric model with an equilibrium temperature of 1315 K, a thick cloud deck ($\alpha_{\rm cloud} = 1.00$), a slight Rayleigh scattering slope in the blue ($\alpha_{\rm haze} = 10$), and hints of a 2.3σ Na I signal at 5893 Å. Within the precision of our observations, we do not detect K I absorption.
3. We compare the observed transmission spectra of HAT-P-1b and WASP-52b, two planetary systems with similar stellar and planetary parameters (Table 6). By constructing optical *HST*/STIS transmission spectra with similar binning schemes (Figure 13), we find that the spectra of these two planets are identical within the uncertainties at optical wavelengths but differ in the near-infrared (Figure 14) based on our best-fit models.
4. The difference in the transmission spectra of WASP-52b and HAT-P-1b from ~1.0 to 5.0 μm may be caused by the presence of an extra optical absorber in the atmosphere of HAT-P-1b (Nikolov et al. 2014) or uncertainties in the best-fitting models, which are isothermal and therefore cannot accurately capture cloud formation.

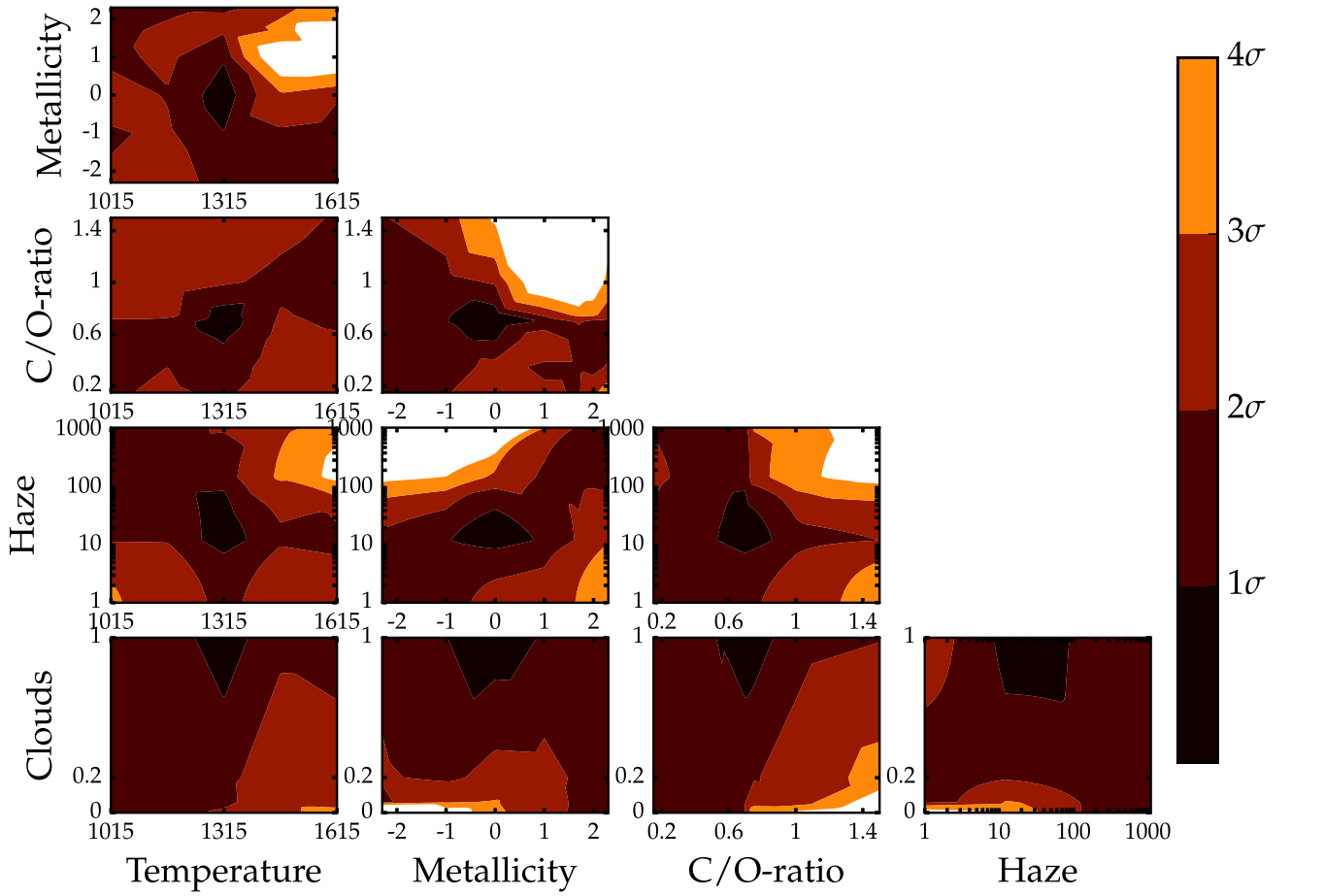

Figure 12. The χ^2 map for WASP-52b for the no-rainout ATMO model grid. The cloud, haze, and metallicity axes are log-scaled. The contours show all combinations of the grid parameters, and the colors indicate the confidence intervals corresponding to the color bar to the right. The white regions correspond to parameter spaces on the grid that are not feasible given current observations at 4σ confidence and can therefore be easily ruled out.

5. Comparative atmospheric observations with *JWST* for WASP-52b and HAT-P-1b will be key to understanding planets with similar system parameters and overlapping atmospheric properties.

In a forthcoming paper, we aim to combine the STIS+*Spitzer* transmission spectrum presented here with existing near-infrared *HST*/WFC3 observations (Bruno et al. 2018). Using the full optical to near-infrared transmission spectrum, we will retrieve the planet's atmospheric properties (G. Bruno et al. 2018, in preparation) to better constrain the atmospheric structure and chemical composition of this inflated hot Jupiter as well as precisely estimate the Na I and K I abundances in the planet's atmosphere. Such an analysis will indicate if comparative planetology and comparative atmospheric studies of WASP-52b with future *JWST* observations will prove insightful.

The authors thank the anonymous referee for helpful comments that greatly improved this manuscript. This paper makes use of observations from the NASA/ESA *Hubble Space Telescope*, obtained at the Space Telescope Science Institute, which is operated by the Association of Universities for Research in Astronomy, Inc., under NASA contract NAS 5-26555. These observations are associated with program GO 14767. The research leading to these results has received funding from the European Research Council under the European Union's Seventh Framework Programme (FP7/2007-2013)/ERC grant agreement 336792. We are thankful to Raphaelle Haywood, James Kirk, Chani Nava, and Ian Weaver for useful discussions.

Table 6
System Parameters and Best-fitting Model Parameters for WASP-52b and HAT-P-1b (Nikolov et al. 2014)

	WASP-52b	HAT-P-1b
Spectral type	K2V	G0V
Stellar mass $M_\star$ $(M_\odot)$	0.87 ± 0.03	1.15 ± 0.05
Stellar radius $R_\star$ $(R_\odot)$	0.79 ± 0.02	1.17 ± 0.03
Surface gravity $\log(g_\star)$ (cgs)	4.58 ± 0.014	4.36 ± 0.01
Stellar temperature $T_{\rm eff}$ (K)	5000 ± 100	5980 ± 50
Metallicity [Fe/H]	0.03 ± 0.12	0.13 ± 0.01
Stellar irradiation I (erg cm^{-2} s^{-1})	$6.5 \pm 0.4 \times 10^8$	$7.0 \pm 0.4 \times 10^8$
$\log(R'_{HK})$	-4.4 ± 0.2	-4.98 ± 0.1
M_p (M_J)	0.434 ± 0.024	0.525 ± 0.019
R_p (R_J)	1.253 ± 0.027	1.319 ± 0.019
ρ (ρ_J)	0.206 ± 0.009	0.213 ± 0.010
Best-fitting ATMO models		
$T_{\rm eq}$ (K)	1315	1322
Fe/H	0.0	1.0
C/O	0.70	0.15
$\alpha_{\rm cloud}$	1.0	0.20
$\alpha_{\rm haze}$	10	10

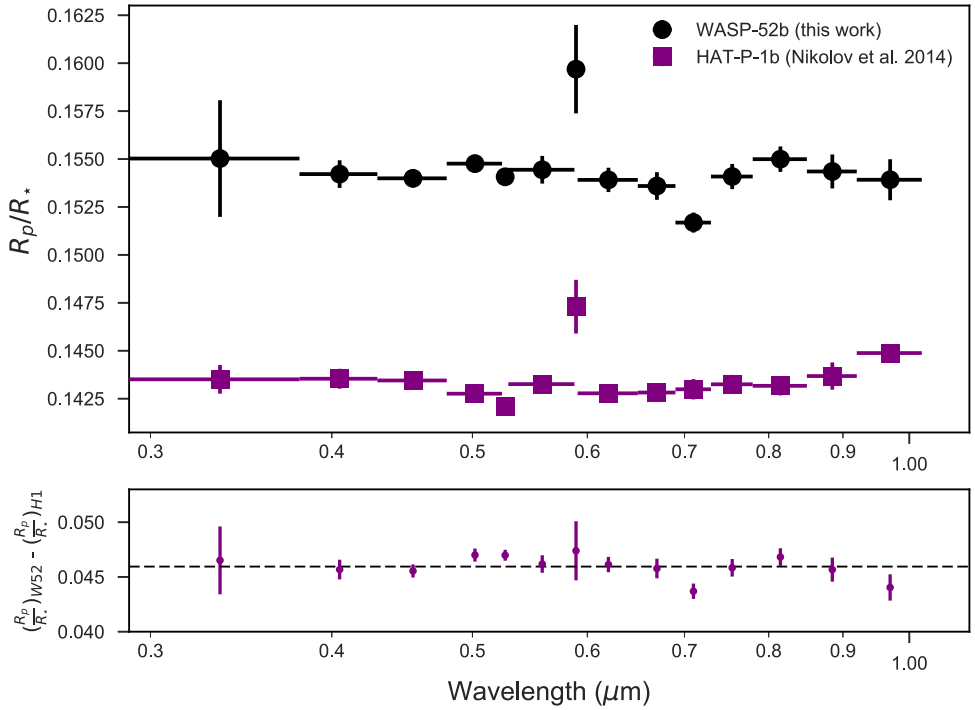

Figure 13. Top panel: comparison of the observed STIS transmission spectra of WASP-52b (black circles) and HAT-P-1b (purple squares; Nikolov et al. 2014) for identical wavelength bins. The HAT-P-1b spectrum is offset by an arbitrary constant such that the first spectroscopic bin is anchored to the first $R_p/R_\star$ value of the WASP-52b spectrum. Bottom panel: difference between the observed WASP-52b spectrum and the offset HAT-P-1b spectrum. The spectra of both planets are identical within the uncertainties (except for one channel at $\sim$0.7 μm), with an average 1σ difference. The horizontal black dashed line indicates the baseline offset between the two spectra.

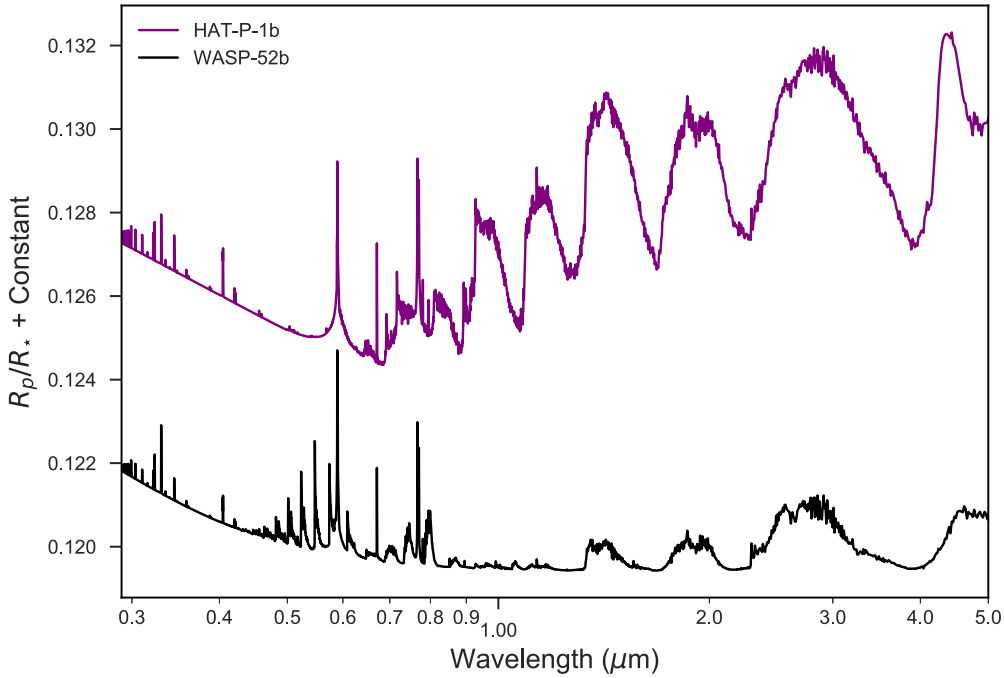

Figure 14. Comparison of the best-fit models for HAT-P-1b (purple) and WASP-52b (black) from $\sim$0.29 to 5 μm. The spectra are identical within the uncertainties at optical wavelengths but differ in the near-infrared.

M.K.A. acknowledges support by the National Science Foundation through a Graduate Research Fellowship. G.W.H. and M.H.W. acknowledge support from Tennessee State University and the State of Tennessee through its Centers of Excellence program. J.S.F. acknowledges funding by the Spanish MINECO grant AYA2016-79425-C3-2-P. J.K.B. acknowledges support from the Royal Astronomical Society. V.B. and D.E. have received funding from the European Research Council (ERC) under the European Unions Horizon 2020 research and innovation program (project Four Aces; grant agreement 724427).

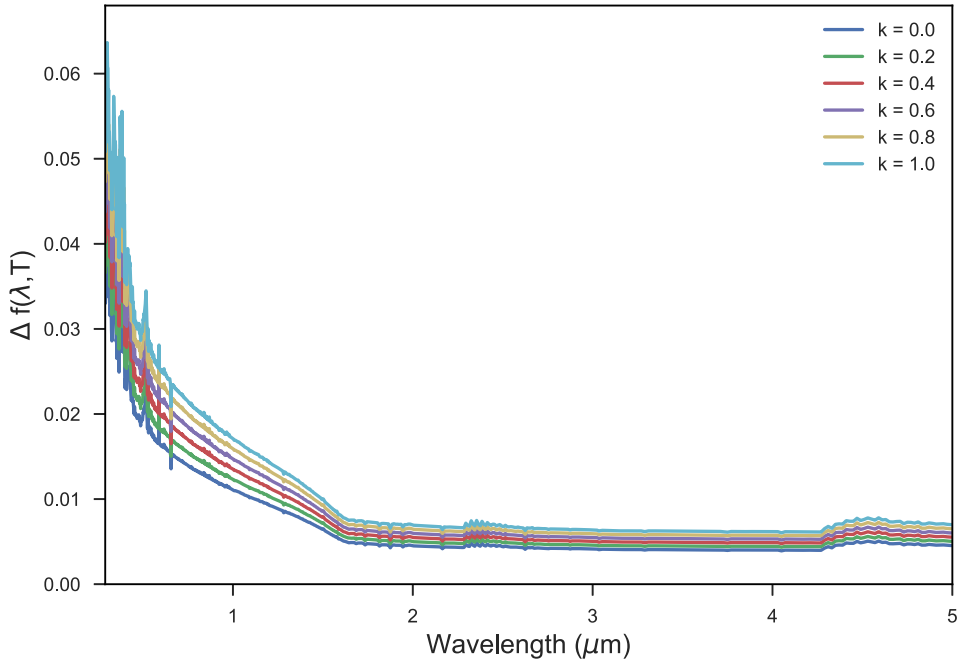

Figure 15. Wavelength-dependent flux correction for a fixed spot temperature (4750 K) and different values of the parameter k, a proxy for the nonspotted fraction of the stellar surface. For the activity correction described in Section 3.4, we assume $k = 1$ (i.e., the spot contribution that the viewer never sees (or always sees) is about the same as the contribution of spots that come into and out of view).

Appendix A
Stellar Activity Correction

A.1. Kernel for GP Regression Model

We used a GP regression to model the ground-based stellar activity monitoring data (Pont et al. 2013; Haywood 2015; Aigrain et al. 2016; Angus et al. 2018). In our GP analysis, we used a three-component kernel of the form $\boldsymbol{K} = k_1 + k_2 + k_3$. The k_1 term models the flexible (quasi-)periodicity of the ground-based activity monitoring data. It is a squared exponential kernel multiplied by an exponential sine squared kernel ($k_1 = A^2\ [k(r^2) \times k(\boldsymbol{x}_i, \boldsymbol{x}_j)]$), where

$$k(r^2) = e^{r^2/2} \tag{5}$$

represents the squared exponential kernel for periodic variations in the time series data parameterized by r. The exponential sine squared kernel is given by

$$k(\boldsymbol{x}_i, \boldsymbol{x}_j) = \exp\left(-\Gamma \sin^2\left[\frac{\pi}{P}|x_i - x_j|\right]\right), \tag{6}$$

where Γ represents the scale of the correlations and P is the period of the oscillations.

The second term, k_2, represents the irregularities in amplitude and period. It is a rational quadratic kernel of the form

$$k_2(r^2) = A^2\left(1 - \frac{r^2}{2\alpha}\right) \tag{7}$$

for amplitude A, Gamma distribution parameter α, and length scale r.

The k_3 term incorporates stellar noise in the GP model and is a squared exponential kernel (of the form shown in Equation (5)) added to a white kernel of the form $k_3(\boldsymbol{x}_i, \boldsymbol{x}_j) = c\delta_{ij}$ for constant c and diagonal value δ_{ij}.

A.2. Deriving the Wavelength-dependent Flux Correction

As described in Section 3, we account for the effects of stellar activity and unocculted starspots on the transmission spectrum by using ground-based photometry and by deriving the wavelength-dependent flux correction $\Delta f(\lambda, T)$ (Sing et al. 2011b; see also Section 3.4, Equation (1)). This correction depends on the parameter k, which provides an assumption for the nonspotted flux on the stellar surface (Aigrain et al. 2012). We fixed k to unity based on Aigrain et al. (2012), who found this value appropriate to use for active stars. Physically, $k = 1$ corresponds to a spot contribution that the viewer never sees (or always sees) that is about the same as the contribution of spots that come into and out of view.

The value of this parameter is based on several assumptions; however, it is, in actuality, very ill constrained, and we warn the reader of the difficulty in selecting a value of k. To explore the potential effect of the choice of k on the final transmission spectrum, we tested different values of this parameter in the range $k = 0$–1 in steps of 0.2 (Figure 15). We find that larger values of k correspond (linearly) to a higher derived flux correction $\Delta f(\lambda, T)$. When applying the activity correction to the binned light curves, we find that the light curves are rescaled to a higher $R_p/R_\star$ baseline if a larger correction is applied. Thus, the parameter k is not wavelength-dependent and therefore does not affect the shape of the slope of the transmission spectrum. Rather, varying the value of k simply shifts the $R_p/R_\star$ baseline of the transmission spectrum vertically.

Appendix B
STIS Light Curves

B.1. STIS White Light Curve Systematics Models

As described in Section 4.1, we detrended instrument systematic effects in the light curves by fitting a fourth-order

Table 7
White Light Curve Systematics Models

	Model
	G430L models
1	$\phi_t + \phi_t^2 + \phi_t^3 + \phi_t^4 + t$
2	$\phi_t + \phi_t^2 + \phi_t^3 + \phi_t^4 + t + \omega + x^2$
3	$\phi_t + \phi_t^2 + \phi_t^3 + \phi_t^4 + t + x + y^2$
4	$\phi_t + \phi_t^2 + \phi_t^3 + \phi_t^4 + t + x^2 + y$
5	$\phi_t + \phi_t^2 + \phi_t^3 + \phi_t^4 + t + \omega$
6	$\phi_t + \phi_t^2 + \phi_t^3 + \phi_t^4 + t + x$
7	$\phi_t + \phi_t^2 + \phi_t^3 + \phi_t^4 + t + y$
8	$\phi_t + \phi_t^2 + \phi_t^3 + \phi_t^4 + t + \omega + \omega^3 + x$
9	$\phi_t + \phi_t^2 + \phi_t^3 + \phi_t^4 + t + \omega + y$
10	$\phi_t + \phi_t^2 + \phi_t^3 + \phi_t^4 + t + \omega + x + y$
11	$\phi_t + \phi_t^2 + \phi_t^3 + \phi_t^4 + t + \omega + \omega^2$
12	$\phi_t + \phi_t^2 + \phi_t^3 + \phi_t^4 + t + \omega + \omega^2 + \omega^3$
13	$\phi_t + \phi_t^2 + \phi_t^3 + \phi_t^4 + t + x + x^2 + y$
14	$\phi_t + \phi_t^2 + \phi_t^3 + \phi_t^4 + t + \omega + x + x^2 + x^3$
15	$\phi_t + \phi_t^2 + \phi_t^3 + \phi_t^4 + t + \omega + y + y^2$
16	$\phi_t + \phi_t^2 + \phi_t^3 + \phi_t^4 + t + \omega + y + y^2 + y^3$
17	$\phi_t + \phi_t^2 + \phi_t^3 + \phi_t^4 + t + \omega + \omega^2 + \omega^3 + x$
18	$\phi_t + \phi_t^2 + \phi_t^3 + \phi_t^4 + t + x + x^2$
19	$\phi_t + \phi_t^2 + \phi_t^3 + \phi_t^4 + t + x + x^2 + x^3$
20	$\phi_t + \phi_t^2 + \phi_t^3 + \phi_t^4 + t + y + y^2$
21	$\phi_t + \phi_t^2 + \phi_t^3 + \phi_t^4 + t + y + y^2 + y^3$
22	$\phi_t + \phi_t^2 + \phi_t^3 + \phi_t^4 + t + \omega + \omega^2 + x$
23	$\phi_t + \phi_t^2 + \phi_t^3 + \phi_t^4 + t + \omega + \omega^2 + x + y$
24	$\phi_t + \phi_t^2 + \phi_t^3 + \phi_t^4 + t + \omega + \omega^2 + x + x^2 + y + y^2$
25	$\phi_t + \phi_t^2 + \phi_t^3 + \phi_t^4 + t + \omega^2 + \omega^3 + x + x^2 + x^3 + y + y^2 + y^3$
	G750L models
1	$\phi_t + \phi_t^2 + \phi_t^3 + \phi_t^4 + t$
2	$\phi_t + \phi_t^2 + \phi_t^3 + \phi_t^4 + t + \omega + x^2$
3	$\phi_t + \phi_t^2 + \phi_t^3 + \phi_t^4 + t + x + y^2$
4	$\phi_t + \phi_t^2 + \phi_t^3 + \phi_t^4 + t + x^2 + y$
5	$\phi_t + \phi_t^2 + \phi_t^3 + \phi_t^4 + t + \omega$
6	$\phi_t + \phi_t^2 + \phi_t^3 + \phi_t^4 + t + x$
7	$\phi_t + \phi_t^2 + \phi_t^3 + \phi_t^4 + t + y$
8	$\phi_t + \phi_t^2 + \phi_t^3 + \phi_t^4 + t + \omega + x$
9	$\phi_t + \phi_t^2 + \phi_t^3 + \phi_t^4 + t + \omega + y$
10	$\phi_t + \phi_t^2 + \phi_t^3 + \phi_t^4 + t + \omega + x + y$
11	$\phi_t + \phi_t^2 + \phi_t^3 + \phi_t^4 + t + \omega + \omega^2$
12	$\phi_t + \phi_t^2 + \phi_t^3 + \phi_t^4 + t + \omega$
13	$\phi_t + \phi_t^2 + \phi_t^3 + \phi_t^4 + t + x + x^2 + y$
14	$\phi_t + \phi_t^2 + \phi_t^3 + \phi_t^4 + t + \omega + x + x^2 + x^3$
15	$\phi_t + \phi_t^2 + \phi_t^3 + \phi_t^4 + t + \omega + y + y^2$
16	$\phi_t + \phi_t^2 + \phi_t^3 + \phi_t^4 + t + \omega + y + y^2 + y^3$
17	$\phi_t + \phi_t^2 + \phi_t^3 + \phi_t^4 + t + \omega + \omega^2 + x$
18	$\phi_t + \phi_t^2 + \phi_t^3 + \phi_t^4 + t + x + x^2$
19	$\phi_t + \phi_t^2 + \phi_t^3 + \phi_t^4 + t + x + x^2 + x^3$
20	$\phi_t + \phi_t^2 + \phi_t^3 + \phi_t^4 + t + y + y^2$
21	$\phi_t + \phi_t^2 + \phi_t^3 + \phi_t^4 + t + y + y^2 + y^3$
22	$\phi_t + \phi_t^2 + \phi_t^3 + \phi_t^4 + t + \omega + \omega^2 + x$
23	$\phi_t + \phi_t^2 + \phi_t^3 + \phi_t^4 + t + \omega + \omega^2 + x + y$
24	$\phi_t + \phi_t^2 + \phi_t^3 + \phi_t^4 + t + \omega + \omega^2 + x + x^2 + y + y^2$
25	$\phi_t + \phi_t^2 + \phi_t^3 + \phi_t^4 + t + \omega + \omega^2 + x + x^3 + y^2 + y^3$

Table 8
Systematics Model Selection for the STIS White Light Curves

Model	χ^2	BIC	n	d.o.f.	i (degrees)	$a/R_\star$	$R_p/R_\star$
Visit 52							
1	46.55	72.92	27	19	85.35	7.60	0.1677
2	43.79	76.74	27	17	85.35	7.60	0.1676
3	34.76	67.72	27	17	85.35	7.60	0.1688
4	30.09	63.05	27	17	85.35	7.60	0.1691
5	45.82	75.48	27	18	85.35	7.60	0.1676
6	36.48	66.15	27	18	85.35	7.60	0.1685
7	30.09	59.76	27	18	85.35	7.60	0.1691
8	33.54	69.80	27	16	85.35	7.60	0.1683
9	29.88	62.84	27	17	85.35	7.60	0.1690
10	29.39	65.64	27	16	85.35	7.60	0.1690
11	43.40	76.36	27	17	85.35	7.60	0.1675
12	42.23	78.48	27	16	85.35	7.60	0.1673
13	29.28	65.54	27	16	85.35	7.60	0.1693
14	32.63	72.18	27	15	85.35	7.60	0.1687
15	25.93	62.18	27	16	85.35	7.60	0.1696
16	24.98	64.53	27	15	85.35	7.60	0.1696
17	33.51	73.06	27	15	85.35	7.60	0.1683
18	34.97	67.93	27	17	85.35	7.60	0.1689
19	34.32	70.57	27	16	85.35	7.60	0.1689
20	26.00	58.96	27	17	85.35	7.60	0.1696
21	25.04	61.30	27	16	85.35	7.60	0.1695
22	33.52	69.78	27	16	85.35	7.60	0.1683
23	29.38	68.93	27	15	85.35	7.60	0.1690
24	25.48	71.62	27	13	85.35	7.60	0.1696
25	24.59	77.32	27	11	85.35	7.60	0.1697
Visit 53							
1	46.30	72.66	27	19	85.35	7.60	0.1656
2	42.60	75.56	27	17	85.35	7.60	0.1655
3	43.78	76.73	27	17	85.35	7.60	0.1654
4	45.11	78.06	27	17	85.35	7.60	0.1658
5	43.80	73.46	27	18	85.35	7.60	0.1655
6	46.04	75.70	27	18	85.35	7.60	0.1657
7	46.09	75.75	27	18	85.35	7.60	0.1657
8	43.27	79.52	27	16	85.35	7.60	0.1656
9	43.70	76.66	27	17	85.35	7.60	0.1655
10	43.30	79.55	27	16	85.35	7.60	0.1656
11	43.61	76.57	27	17	85.35	7.60	0.1660
12	43.54	79.79	27	16	85.35	7.60	0.1659
13	44.95	81.21	27	16	85.35	7.60	0.1658
14	33.46	73.01	27	15	85.35	7.60	0.1659
15	41.64	77.90	27	16	85.35	7.60	0.1653
16	41.60	81.15	27	15	85.35	7.60	0.1653
17	43.25	82.80	27	15	85.35	7.60	0.1658
18	45.27	78.23	27	17	85.35	7.60	0.1657
19	40.70	76.95	27	16	85.35	7.60	0.1659
20	43.61	76.57	27	17	85.35	7.60	0.1654
21	43.33	79.59	27	16	85.35	7.60	0.1653
22	43.29	79.54	27	16	85.35	7.60	0.1658
23	43.26	82.81	27	15	85.35	7.60	0.1657
24	38.82	84.96	27	13	85.35	7.60	0.1658
25	26.00	78.73	27	11	85.35	7.60	0.1689
Visit 54							
1	58.65	81.73	27	20	85.35	7.60	0.1681
2	50.54	80.20	27	18	85.35	7.60	0.1684
3	45.06	74.72	27	18	85.35	7.60	0.1671
4	54.79	84.45	27	18	85.35	7.60	0.1685
5	51.13	77.50	27	19	85.35	7.60	0.1682
6	48.52	74.89	27	19	85.35	7.60	0.1673
7	56.89	83.26	27	19	85.35	7.60	0.1681
8	38.76	68.42	27	18	85.35	7.60	0.1673
9	46.54	76.20	27	18	85.35	7.60	0.1681
10	35.87	68.83	27	17	85.35	7.60	0.1674
11	49.75	79.41	27	18	85.35	7.60	0.1681

Table 8
(Continued)

Model	χ^2	BIC	n	d.o.f.	i (degrees)	$a/R_\star$	$R_p/R_\star$
12	51.13	77.50	27	19	85.35	7.60	0.1682
13	46.63	79.59	27	17	85.35	7.60	0.1678
14	33.56	69.82	27	16	85.35	7.60	0.1669
15	46.18	79.14	27	17	85.35	7.60	0.1681
16	45.65	81.90	27	16	85.35	7.60	0.1681
17	38.75	71.71	27	17	85.35	7.60	0.1673
18	47.33	76.99	27	18	85.35	7.60	0.1677
19	41.75	74.70	27	17	85.35	7.60	0.1672
20	56.75	86.41	27	18	85.35	7.60	0.1680
21	56.24	89.20	27	17	85.35	7.60	0.1681
22	38.75	71.71	27	17	85.35	7.60	0.1673
23	35.87	72.12	27	16	85.35	7.60	0.1674
24	30.89	73.73	27	14	85.35	7.60	0.1670
25	26.00	68.84	27	14	85.35	7.60	0.1675

polynomial to the flux dependence on *HST* orbital phase. Each model represents a unique linear combination of the detrending variables: orbital phase (ϕ_t), drift of the spectra on the detector (x and y), the shift (ω) of each stellar spectrum cross-correlated with the first spectrum of the time series, and time t. The variables x and y are the trace slope and an offset in the cross dispersion direction, respectively. The parameter ω is measured by cross-correlating a reference spectrum with the remaining spectra and is measured prior to resampling the spectra.

For both the G430L and G750L STIS observations, we used the 25 systematics models listed in Table 7 to detrend the light curves. After performing separate fits for each model, we marginalized over the entire set of systematics models assuming equally weighted priors to select which systematics model to use. Table 8 summarizes the selection of systematics models based on the STIS white light curves. We selected the model for detrending based on the lowest Aikake Information Criterion value.

B.2. STIS Spectrophotometric Light Curves

The broadband STIS+*Spitzer* transmission spectrum for WASP-52b reported in Table 5 gives the weighted mean of the two STIS G430L observations (visits 52 and 53). In Tables 9 and 10, we report the spectrophotometric light curves for each G430L visit. To produce the raw transmission spectrum from the spot-corrected spectrum, the reader may simply reverse the correction given in Table 3 on each transit observation separately.

Table 9
STIS G430L (Visit 52) Transmission Spectrum Results for WASP-52b

λ (Å)	$(R_p/R_*)_{\rm uncorr}$	$(R_p/R_*)_{\rm corr}$	c_1	c_2	c_3	c_4
2900–3700	0.15814 ± 0.00712	0.17008 ± 0.00444	0.4371	−0.7679	1.6319	−0.3645
3700–3950	0.16152 ± 0.00285	0.16801 ± 0.00294	0.7648	−1.1573	1.7190	−0.4157
3950–4113	0.16997 ± 0.00300	0.16293 ± 0.00181	0.4778	−0.6459	1.6564	−0.5511
4113–4250	0.16770 ± 0.00162	0.16633 ± 0.00128	0.4831	−0.6750	1.7025	−0.5879
4250–4400	0.16683 ± 0.00151	0.16379 ± 0.00175	0.6151	−0.8347	1.7798	−0.6519
4400–4500	0.16366 ± 0.00144	0.16739 ± 0.00175	0.4691	−0.4858	1.5912	−0.6570
4500–4600	0.16610 ± 0.00151	0.16536 ± 0.00170	0.4777	−0.4094	1.5029	−0.6494
4600–4700	0.16833 ± 0.00108	0.16574 ± 0.00158	0.5977	−0.6932	1.6924	−0.6811
4700–4800	0.16453 ± 0.00191	0.16496 ± 0.00150	0.4411	−0.2389	1.1548	−0.4505
4800–4900	0.16528 ± 0.00117	0.16532 ± 0.00134	0.5159	−0.3136	1.2538	−0.5560
4900–5000	0.16317 ± 0.00159	0.16626 ± 0.00176	0.4399	−0.1314	1.0138	−0.4335
5000–5100	0.16720 ± 0.00107	0.16696 ± 0.00135	0.5409	−0.3989	1.1899	−0.4566
5100–5200	0.16898 ± 0.00178	0.16612 ± 0.00159	0.5605	−0.4363	1.0910	−0.3757
5200–5300	0.16782 ± 0.00104	0.16525 ± 0.00103	0.5381	−0.2913	1.0934	−0.4736
5300–5400	0.16556 ± 0.00116	0.16470 ± 0.00200	0.5732	−0.3581	1.1751	−0.5264
5400–5500	0.16641 ± 0.00133	0.16719 ± 0.00122	0.5975	−0.4018	1.1388	−0.4758
5500–5600	0.16496 ± 0.00110	0.16675 ± 0.00124	0.6370	−0.4886	1.2206	−0.5147
5600–5700	0.16367 ± 0.00156	0.16527 ± 0.00101	0.5662	−0.2476	0.9413	−0.4076

Table 10
STIS G430L (Visit 53) Transmission Spectrum Results for WASP-52b

λ (Å)	$(R_p/R_*)_{\rm uncorr}$	$(R_p/R_*)_{\rm corr}$	c_1	c_2	c_3	c_4
2900–3700	0.15814 ± 0.00712	0.15421 ± 0.00677	0.4371	−0.7679	1.6319	−0.3645
3700–3950	0.16152 ± 0.00285	0.15781 ± 0.00296	0.7648	−1.1573	1.7190	−0.4157
3950–4113	0.16997 ± 0.00300	0.16681 ± 0.00296	0.4778	−0.6459	1.6564	−0.5511
4113–4250	0.16770 ± 0.00162	0.16457 ± 0.00159	0.4831	−0.6750	1.7025	−0.5879
4250–4400	0.16683 ± 0.00151	0.16394 ± 0.00148	0.6151	−0.8347	1.7798	−0.6519
4400–4500	0.16366 ± 0.00144	0.16101 ± 0.00142	0.4691	−0.4858	1.5912	−0.6570
4500–4600	0.16610 ± 0.00151	0.16358 ± 0.00149	0.4777	−0.4094	1.5029	−0.6494
4600–4700	0.16833 ± 0.00108	0.16583 ± 0.00106	0.5977	−0.6932	1.6924	−0.6811
4700–4800	0.16453 ± 0.00191	0.16211 ± 0.00187	0.4411	−0.2389	1.1548	−0.4505
4800–4900	0.16528 ± 0.00117	0.16290 ± 0.00115	0.5159	−0.3136	1.2538	−0.5560
4900–5000	0.16317 ± 0.00159	0.16079 ± 0.00156	0.4399	−0.1314	1.0138	−0.4335
5000–5100	0.16720 ± 0.00107	0.16463 ± 0.00105	0.5409	−0.3989	1.1899	−0.4566
5100–5200	0.16898 ± 0.00178	0.16623 ± 0.00175	0.5605	−0.4363	1.0910	−0.3757
5200–5300	0.16782 ± 0.00104	0.16541 ± 0.00103	0.5381	−0.2913	1.0934	−0.4736
5300–5400	0.16556 ± 0.00116	0.16330 ± 0.00114	0.5732	−0.3581	1.1751	−0.5264
5400–5500	0.16641 ± 0.00133	0.16416 ± 0.00132	0.5975	−0.4018	1.1388	−0.4758
5500–5600	0.16496 ± 0.00110	0.16279 ± 0.00108	0.6370	−0.4886	1.2206	−0.5147
5600–5700	0.16367 ± 0.00156	0.16157 ± 0.00154	0.5662	−0.2476	0.9413	−0.4076

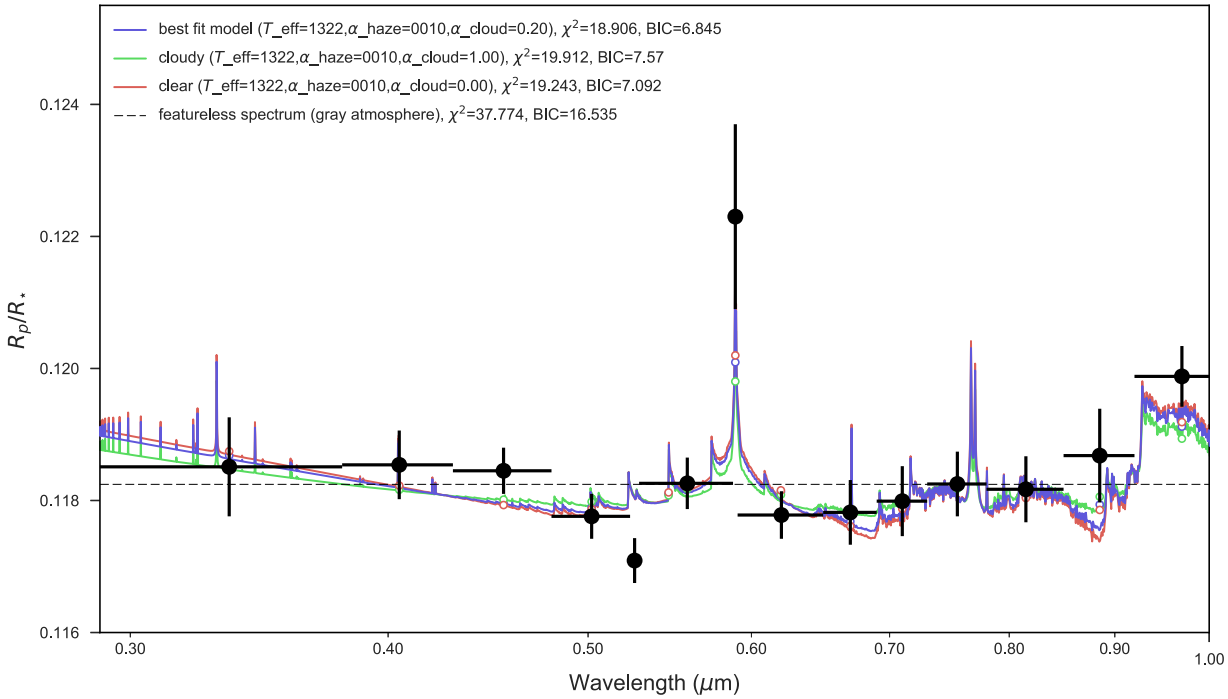

Figure 16. *HST*/STIS transmission spectrum of HAT-P-1b (black points; Nikolov et al. 2014) compared to a subset of the best-fit theoretical atmospheric models (lines) for the no-rainout ATMO grid. For reference, the dashed black line shows the average $R_p/R_\star$ baseline of the transmission spectrum.

Appendix C
HAT-P-1b Forward Model Fits

Figure 16 shows the *HST*/STIS transmission spectrum of the well-studied inflated hot Jupiter HAT-P-1b from Nikolov et al. (2014) compared to the best-fitting theoretical forward model from the ATMO grid generated for the parameters of HAT-P-1b[20] in addition to representative clear and cloudy models. We performed these fits using the procedure described in Section 5.2. We find that the best-fit model has $T = 1322$ K with a strong Na I signal and is slightly cloudy ($\alpha_{\rm cloud} = 0.20$) and hazy ($\alpha_{\rm haze} = 10$).

ORCID iDs

Munazza K. Alam https://orcid.org/0000-0003-4157-832X
Nikolay Nikolov https://orcid.org/0000-0002-6500-3574
Mercedes López-Morales https://orcid.org/0000-0003-3204-8183
Gregory W. Henry https://orcid.org/0000-0003-4155-8513
Jorge Sanz-Forcada https://orcid.org/0000-0002-1600-7835
Hannah R. Wakeford https://orcid.org/0000-0003-4328-3867
Kevin B. Stevenson https://orcid.org/0000-0002-7352-7941
Nikole K. Lewis https://orcid.org/0000-0002-8507-1304
Joanna K. Barstow https://orcid.org/0000-0003-3726-5419
Vincent Bourrier https://orcid.org/0000-0002-9148-034X
Lars A. Buchhave https://orcid.org/0000-0003-1605-5666
David Ehrenreich https://orcid.org/0000-0001-9704-5405
Antonio García Muñoz https://orcid.org/0000-0003-1756-4825

[20] https://bd-server.astro.ex.ac.uk/exoplanets/HAT-P-01/

References

Aigrain, S., Parviainen, H., & Pope, B. J. S. 2016, MNRAS, 459, 2408
Aigrain, S., Pont, F., & Zucker, S. 2012, MNRAS, 419, 3147
Akaike, H. 1974, ITAC, 19, 716
Ambikasaran, S., Foreman-Mackey, D., Greengard, L., Hogg, D. W., & O'Neil, M. 2015, ITPAM, 38, 252
Amundsen, D. S., Baraffe, I., Tremblin, P., et al. 2014, A&A, 564, A59
Angus, R., Morton, T., Aigrain, S., Foreman-Mackey, D., & Rajpaul, V. 2018, MNRAS, 474, 2094
Berdyugina, S. V. 2005, LRSP, 2, 8
Bourrier, V., Lecavelier des Etangs, A., Dupuy, H., et al. 2013, A&A, 551, A63
Brown, T. M. 2001, ApJ, 553, 1006
Bruno, G., Lewis, N. K., Stevenson, K. B., et al. 2018, AJ, 156, 124
Burrows, A., Rauscher, E., Spiegel, D. S., & Menou, K. 2010, ApJ, 719, 341
Carter, J. A., & Winn, J. N. 2009, ApJ, 704, 51
Charbonneau, D., Allen, L. E., Megeath, S. T., et al. 2005, ApJ, 626, 523
Charbonneau, D., Brown, T. M., Noyes, R. W., & Gilliland, R. L. 2002, ApJ, 568, 377
Charbonneau, D., Knutson, H. A., Barman, T., et al. 2008, ApJ, 686, 1341
Chen, G., Pallé, E., Nortmann, L., et al. 2017, A&A, 600, L11
Claret, A. 2000, A&A, 363, 1081
Dang, L., Cowan, N. B., Schwartz, J. C., et al. 2018, NatAs, 2, 220
Deming, D., Seager, S., Richardson, L. J., & Harrington, J. 2005, Natur, 434, 740
Désert, J.-M., Vidal-Madjar, A., Lecavelier Des Etangs, A., et al. 2008, A&A, 492, 585
Drummond, B., Tremblin, P., Baraffe, I., et al. 2016, A&A, 594, A69
Evans, T. M., Sing, D. K., Kataria, T., et al. 2017, Natur, 548, 58
Fazio, G. G., Hora, J. L., Allen, L. E., et al. 2004, ApJS, 154, 10
Fortney, J. J., Shabram, M., Showman, A. P., et al. 2010, ApJ, 709, 1396
Fruscione, A., McDowell, J. C., Allen, G. E., et al. 2006, Proc. SPIE, 6270, 62701V
Gaia Collaboration, Brown, A. G. A., Vallenari, A., et al. 2018, arXiv:1804.09365
Gibson, N. P. 2014, MNRAS, 445, 3401
Gibson, N. P., Nikolov, N., Sing, D. K., et al. 2017, MNRAS, 467, 4591
Gilliland, R. L., Goudfrooij, P., & Kimble, R. A. 1999, PASP, 111, 1009
Goyal, J. M., Mayne, N., Sing, D. K., et al. 2018, MNRAS, 474, 5158
Grillmair, C. J., Burrows, A., Charbonneau, D., et al. 2008, Natur, 456, 767
Haywood, R. D. 2015, PhD thesis, Univ. St Andrews

Haywood, R. D., Collier Cameron, A., Queloz, D., et al. 2014, MNRAS, 443, 2517
Hébrard, G., Collier Cameron, A., Brown, D. J. A., et al. 2013, A&A, 549, A134
Houck, J. C., & Denicola, L. A. 2000, in ASP Conf. Ser. 216, Astronomical Data Analysis Software and Systems IX, ed. N. Manset, C. Veillet, & D. Crabtree (San Francisco, CA: ASP), 591
Huitson, C. M., Désert, J.-M., Bean, J. L., et al. 2017, AJ, 154, 95
Huitson, C. M., Sing, D. K., Pont, F., et al. 2013, MNRAS, 434, 3252
Huitson, C. M., Sing, D. K., Vidal-Madjar, A., et al. 2012, MNRAS, 422, 2477
Jordán, A., Espinoza, N., Rabus, M., et al. 2013, ApJ, 778, 184
Kirk, J., Wheatley, P. J., Louden, T., et al. 2016, MNRAS, 463, 2922
Knutson, H. A., Charbonneau, D., Allen, L. E., et al. 2007, Natur, 447, 183
Knutson, H. A., Charbonneau, D., Allen, L. E., Burrows, A., & Megeath, S. T. 2008, ApJ, 673, 526
Knutson, H. A., Lewis, N., Fortney, J. J., et al. 2012, ApJ, 754, 22
Kochanek, C. S., Shappee, B. J., Stanek, K. Z., et al. 2017, PASP, 129, 104502
Kreidberg, L. 2017, in Handbook of Exoplanets, ed. H. J. Deeg & J. A. Belmonte (Berlin: Springer), 100
Kreidberg, L., Bean, J. L., Désert, J.-M., et al. 2014, Natur, 505, 69
Kurucz, R. L. 1993, yCat, 6039, 0
Lecavelier Des Etangs, A., Ehrenreich, D., Vidal-Madjar, A., et al. 2010, A&A, 514, A72
Lecavelier Des Etangs, A., Vidal-Madjar, A., Désert, J.-M., & Sing, D. 2008, A&A, 485, 865
Lewis, N. K., Knutson, H. A., Showman, A. P., et al. 2013, ApJ, 766, 95
Louden, T., Wheatley, P. J., Irwin, P. G. J., Kirk, J., & Skillen, I. 2017, arXiv:1703.09285
Magic, Z., Chiavassa, A., Collet, R., & Asplund, M. 2015, A&A, 573, A90
Mallonn, M., Bernt, I., Herrero, E., et al. 2016, MNRAS, 463, 604
Mancini, L., Southworth, J., Raia, G., et al. 2017, MNRAS, 465, 843
Mandel, K., & Agol, E. 2002, ApJL, 580, L171
Markwardt, C. B. 2009, in ASP Conf. Ser. 411, Astronomical Data Analysis Software and Systems XVIII, ed. D. A. Bohlender, D. Durand, & P. Dowler (San Francisco, CA: ASP), 251
Marley, M. S., Ackerman, A. S., Cuzzi, J. N., & Kitzmann, D. 2013, in Comparative Climatology of Terrestrial Planets, ed. S. J. Mackwell et al. (Tucson, AZ: Univ. Arizona Press), 367
Mighell, K. J. 2005, MNRAS, 361, 861
Nikolov, N., Sing, D. K., Burrows, A. S., et al. 2015, MNRAS, 447, 463
Nikolov, N., Sing, D. K., Fortney, J. J., et al. 2018, Natur, 557, 526
Nikolov, N., Sing, D. K., Gibson, N. P., et al. 2016, ApJ, 832, 191
Nikolov, N., Sing, D. K., Pont, F., et al. 2014, MNRAS, 437, 46
Pont, F., Sing, D. K., Gibson, N. P., et al. 2013, MNRAS, 432, 2917
Reach, W. T., Megeath, S. T., Cohen, M., et al. 2005, PASP, 117, 978
Seager, S., & Sasselov, D. D. 2000, ApJ, 537, 916
Shappee, B. J., Prieto, J. L., Grupe, D., et al. 2014, ApJ, 788, 48
Sing, D. K. 2010, A&A, 510, A21
Sing, D. K., Désert, J.-M., Fortney, J. J., et al. 2011a, A&A, 527, A73
Sing, D. K., Désert, J.-M., Lecavelier Des Etangs, A., et al. 2009, A&A, 505, 891
Sing, D. K., Fortney, J. J., Nikolov, N., et al. 2016, Natur, 529, 59
Sing, D. K., Lecavelier des Etangs, A., Fortney, J. J., et al. 2013, MNRAS, 436, 2956
Sing, D. K., & López-Morales, M. 2009, A&A, 493, L31
Sing, D. K., Pont, F., Aigrain, S., et al. 2011b, MNRAS, 416, 1443
Sing, D. K., Vidal-Madjar, A., Désert, J.-M., Lecavelier des Etangs, A., & Ballester, G. 2008a, ApJ, 686, 658
Sing, D. K., Vidal-Madjar, A., Lecavelier des Etangs, A., et al. 2008b, ApJ, 686, 667
Sing, D. K., Wakeford, H. R., Showman, A. P., et al. 2015, MNRAS, 446, 2428
Snellen, I. A. G., Albrecht, S., de Mooij, E. J. W., & Le Poole, R. S. 2008, A&A, 487, 357
Stevenson, K. B. 2016, ApJL, 817, L16
Stevenson, K. B., Line, M. R., Bean, J. L., et al. 2017, AJ, 153, 68
Struve, O. 1952, Obs, 72, 199
Sudarsky, D., Burrows, A., & Hubeny, I. 2003, ApJ, 588, 1121
Todorov, K. O., Deming, D., Knutson, H. A., et al. 2013, ApJ, 770, 102
Tremblin, P., Amundsen, D. S., Chabrier, G., et al. 2016, ApJL, 817, L19
Tremblin, P., Amundsen, D. S., Mourier, P., et al. 2015, ApJL, 804, L17
Vidal-Madjar, A., Lecavelier des Etangs, A., Désert, J.-M., et al. 2003, Natur, 422, 143
Wakeford, H. R., Sing, D. K., Deming, D., et al. 2013, MNRAS, 435, 3481
Wakeford, H. R., Sing, D. K., Deming, D., et al. 2018, AJ, 155, 29
Wakeford, H. R., Sing, D. K., Kataria, T., et al. 2017, Sci, 356, 628
Werner, M. W., Roellig, T. L., Low, F. J., et al. 2004, ApJS, 154, 1
Winn, J. N. 2010, arXiv:1001.2010
Wyttenbach, A., Ehrenreich, D., Lovis, C., Udry, S., & Pepe, F. 2015, A&A, 577, A62
Wyttenbach, A., Lovis, C., Ehrenreich, D., et al. 2017, A&A, 602, A36